Critical Role of Interface and Crystallinity on the Performance and Photostability of Perovskite Solar Cell on Nickel Oxide

Wanyi Nie, Hsinhan Tsai, Jean-Christophe Blancon, Fangze Liu, Costas C Stoumpos, Boubacar Traoré, Mikael Kepenekian, Olivier Durand, Claudine Katan, Sergei Tretiak, et al.

https://doi.org/10.1002/adma.201703879
Advanced Materials, 30, 5, 1703879 (2018)

Critical Role of Interface and Crystallinity on the Performance and Photo-Stability of Perovskite Solar Cell on Nickel Oxide

Wanyi Nie[1*], Hsinhan Tsai[1, 2], Jean-Christophe Blancon[3], Fangze Liu[1], Costas Stoumpos[4], Boubacar Traore[7], Mikael Kepenekian[7], Olivier Durand[6], Claudine Katan[7], Sergei Tretiak[5], Jared Crochet[1], Pulickel M. Ajayan[2], Mercouri Kanatzidis[4], Jacky Even[6] and Aditya D. Mohite[1*]

[1] Materials Physics and Application, Los Alamos National Laboratory, Los Alamos, New Mexico 87545, USA

[2]Materials Science and Nano-engineering, Rice University, Houston, Texas 77005, United States

[3] Physical Chemistry and Applied Spectroscopy Division, Los Alamos National Laboratory, Los Alamos, New Mexico 87545, USA

[4] Department of Chemistry, Department of Materials Science and Engineering and Argonne-Northwestern Solar Energy Research (ANSER) Center, Northwestern University, Evanston, IL 60208, USA.

[5] Theoretical Chemistry and Molecular Physics Division, Los Alamos National Laboratory, Los Alamos, New Mexico 87545, USA

[6] Univ Rennes, Institut FOTON, ISCR UMR 6082, CNRS, Université de Rennes 1, 35042 Rennes, France

[7] Univ Rennes, Institut des Sciences Chimiques de Rennes, ISCR UMR 6226, CNRS, Université de Rennes 1, 35042 Rennes, France

Correspondence: wanyi@lanl.gov and amohite@lanl.gov

Hybrid perovskites are on a trajectory towards realizing the most efficient single-junction, solution-processed photovoltaic devices. However, a critical issue is the limited understanding of the correlation between the degree of crystallinity and the emergent perovskite/hole (or electron) transport layer on device performance and photo-stability. Here we show that the controlled growth of hybrid perovskites on nickel oxide (NiO), results in the formation of thin-films with enhanced crystallinity with characteristic peak width and splittings reminiscent of the tetragonal phase in single-crystals. Photo-physical and interface sensitive measurements reveal a reduced trap density at the perovskite/NiO interface in comparison with perovskites grown on PEDOT: PSS with the same growth conditions. Photovoltaic cells exhibit a high open circuit voltage (1.12 V), indicating a near-ideal energy band-alignment. Moreover, we observe photo-stability of photovoltaic devices up to 10-Suns,

https://doi.org/10.1002/adma.201703879
Advanced Materials, 30, 5, 1703879 (2018)

which is a direct result of the superior crystallinity of perovskite thin-films on NiO. These results elucidate the critical role of the quality of the perovskite/HTL interface in rendering high-performance and photo-stable optoelectronic devices.

Among all the solution-processed thin-film optoelectronic material technologies investigated over the past two decades, organic-inorganic (or hybrid) methylammonium lead tri-iodide ($MAPbI_3$) perovskites have emerged as clear front-runners with proof-of-concept high performance devices demonstrated for a broad range of applications[1-8]. The $MAPbI_3$ based photovoltaic devices have demonstrated constantly increasing power conversion efficiency (PCE), which now exceeds 22%[9,10] and is steadily approaching that of single-junction monocrystalline Silicon (c-Si) solar cells. Although the record for the highest efficiency perovskite solar cell was achieved using a mesoporous Titania (TiO_2) based architecture[10-12], photovoltaic devices employing a simple planar architecture are closing in with the highest reported efficiency of 20%[6,13-15]. Great efforts have been put forth for achieving highly efficient planar solar cell by exploring for potential ideal contact layers[16]. In addition, it is now realized that the next steps in advancing hybrid perovskite based materials towards a viable photovoltaic technology will require simultaneously improving both the overall efficiency and also intrinsic stability. Therefore, optimal selection of electron and hole transport layers will require close consideration such that they not only boost the efficiency but also impart stability against constant full spectrum solar irradiation and environmental effects. Moreover, there is also a stronger consensus that effects such as hysteresis[17-19], ion migration[20-24] and structural instability[25,2623,24] with light soaking are strongly correlated to the degree of crystallinity of the hybrid perovskite thin-films, grain boundaries and interface passivation[21,22,26-29].

There have been a few encouraging reports on using metal oxides as electron and hole transport layers, while improving the charge transport properties in devices, those oxides were

https://doi.org/10.1002/adma.201703879
Advanced Materials, 30, 5, 1703879 (2018)

found to act as protective barriers against the environment[30-35]. For instance, Han and co-workers showed that using modified compact TiO_2 as the electron transport layer (ETL) and NiO_x as the hole transport layer (HTL) resulted in much improved stability for devices when encapsulated with glass[36]. More recently, You el al., showed that using NiO_x as a HTL can lead to much improved stability against water and oxygen when the devices were stored in the dark[37]. Kim et al reported similar results, where Cu doped NiO_x resulted in improved stability for devices stored in the dark[38]. These reports demonstrate the potential of metal oxide films as charge transport layers for high performance photovoltaics that improve protection from the environmental conditions. However, several fundamental questions remain unanswered. For example, there have been no studies investigating the role of crystallinity, structure and the resulting interface quality of $MAPbI_3$ thin-films grown on top of metal oxide layers, which are critical for both performance and stability. Moreover, in most cases, the environmental stability was evaluated by storing the devices in the dark without constant light soaking. There have been several studies have now suggested that constant light soaking is critical for evaluating device stability during operation and cause severe photo degradation due to local phase segregation[26] or electronic trap states or vacancy formation[29,37,39-41]. In fact in our recent work[42], using the poly(3,4-ethylene dioxy thiophene) polystyrene sulfonate (PEDOT:PSS) based planar photovoltaic devices, we showed that constant light soaking with calibrated 1-Sun light source triggers reversible photocurrent degradation within an hour and due to formation of light-activated trap states that are initialized at the interface between the perovskite/HTM or at defects within the bulk film.

Here we demonstrate that perovskite thin-films grown on Li doped NiO (LiNiO) by hot-casting method[43,44] exhibit enhanced crystallinity and structural ordering reminiscent of single crystalline perovskites. In-depth analyses on crystallography and film morphology studies reveal

https://doi.org/10.1002/adma.201703879
Advanced Materials, 30, 5, 1703879 (2018)
the formation of a highly crystalline and characteristic peak splitting indicative of a stabilized tetragonal phase of $MAPbI_3$ unique to single crystalline perovskites with comparable Bragg peak broadenings. We show that the overall quality of the hot-casted perovskite film on LiNiO and the emergent interface is strongly correlated to the observation of reproducible, hysteresis free, high-efficiency devices with an average efficiency of ~17% (active area 0.5 cm^2) mainly arising from a substantial enhancement in the average V_{OC} from ~ 0.9 V to ~1.10 V. Extensive spectroscopy and device characterization reveals the suppression of the non-radiative decay through deep-level traps and improved transport of charge carriers through the bulk and the interfacial contacts. A direct implication of enhanced crystallinity and reduced interface trap density is the suppression of the photo-degradation process usually observed with device using PEDOT: PSS as HTL[42] or less crystalline thin films on LiNiO (grown using a two-step process), thus imparting the much-desired intrinsic photo-stability under continuous light soaking and up to 10-Suns without any UV filter.

Results and discussion

Thin film crystallography and morphology characterization

Figure 1 illustrates the thin-film morphology and crystallinity of $MAPbI_3$ thin film (310 nm~370 nm) grown on top of LiNiO layer by hot-casting method (see SI method section for preparation details) using Scanning Electron Microscopy (SEM), Grazing Incidence X-ray diffraction (GIXRD). As a comparison, we also deposit $MAPbI_3$ on top of PEDOT: PSS (40 nm) under identical casting conditions with comparable perovskite film thicknesses of ~310-370 nm determined using thin-film profilometry and cross-sectional SEM image as illustrated in Fig. 1b. We emphasize that in contrast to other methods for the growth of perovskite thin-films, the hot-cast $MAPbI_3$ on the substrates (both LiNiO and PEDOT:PSS) forms a bulk-like thin-film with no

https://doi.org/10.1002/adma.201703879
Advanced Materials, 30, 5, 1703879 (2018)
apparent grain boundaries traversing through the film thickness and extends uniformly in the lateral direction thus making it ideal for the fabrication of planar solar cells.

https://doi.org/10.1002/adma.201703879
Advanced Materials, 30, 5, 1703879 (2018)

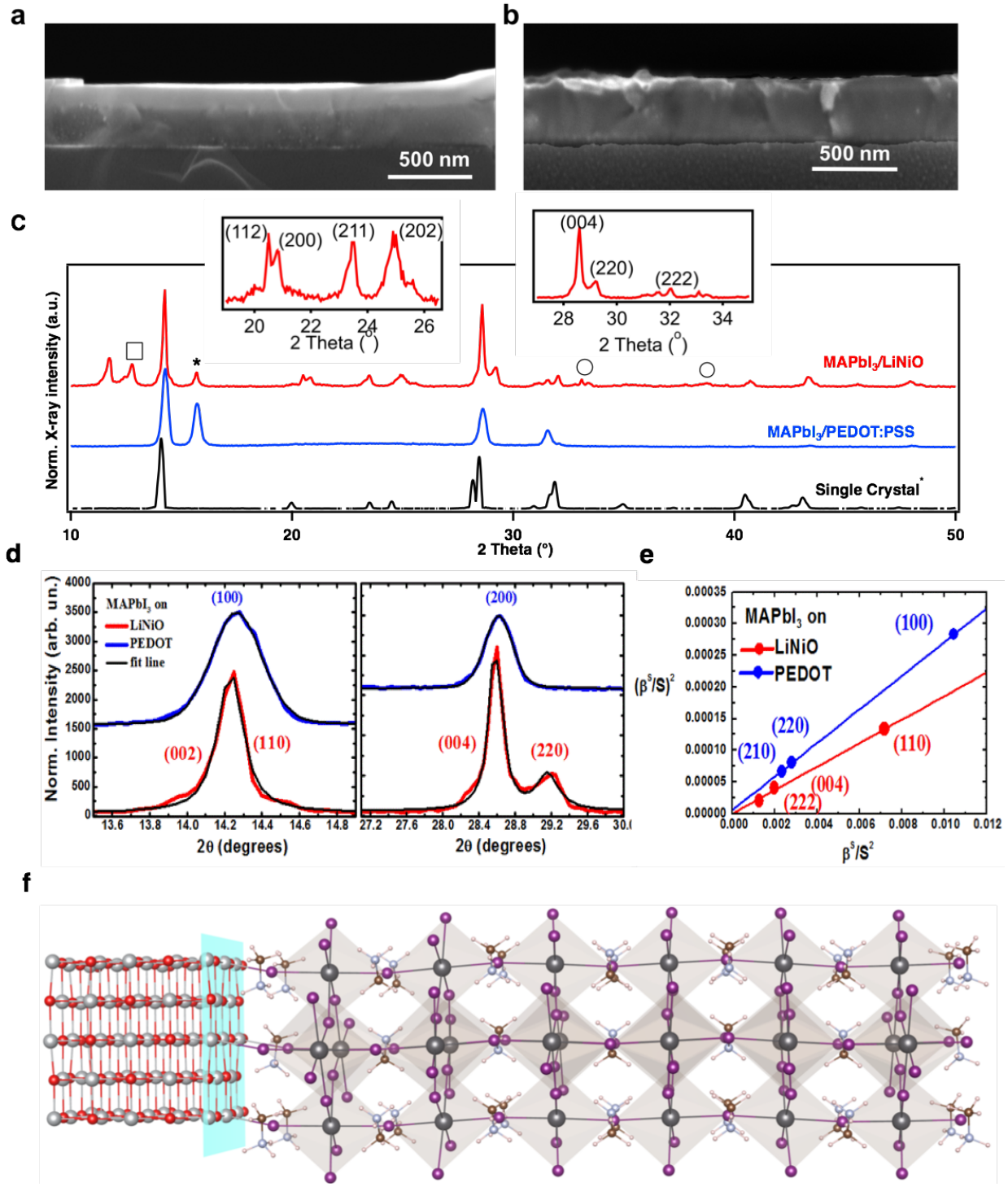

Figure 1. Thin-film characterization illustrating highly crystalline tetragonal phase of $MAPbI_3$. a-b, cross-sectional view of hybrid perovskite thin film by hot-casting method on LiNiO and PEDOT:PSS coated substrates respectively**; c,** GIXRD pattern for $MAPbI_3$ hot-cast thin-film on LiNiO as compared with on PEDOT:PSS substrates and single crystal diffraction pattern [taken

https://doi.org/10.1002/adma.201703879
Advanced Materials, 30, 5, 1703879 (2018)
from reference[45]]with indexing. Insets are zoomed in pattern in a specific range. The peaks labeled with * refer to $MAPbCl_3$ phase and □ are PbI_2 phase, **o** are peaks from LiNiO substrates (see also GIWAXS line cuts in Figure S10); **d**, Zoom-in profiles for (100) and (200) peaks (on PDOT-PSS: labelled using the cubic phase indexation, while on LiNiO, the peaks are labelled using the tetragonal phase indexation) for line profile (Integral Breadths-IB) analysis with pseudo-Voigt fits taking into account $\lambda_{K\alpha_1}$ and $\lambda_{K\alpha_2}$ wavelengths, **e,** IB analysis using Halder-Wagner plots[46,47], where β is the integral breadth of the diffraction peak and S is defined as $S = \frac{2\sin\theta}{\lambda}$. **f,** Structure of the $MAPbI_3$/NiO (100) model interface based on DFT calculations. The structure shows Ni-I bonds at the interface region. For the colors, red for O, gray for Ni, purple for I, light blue for N, brown for C and pink for H.

The crystallinity of the perovskite film was then characterized using GIXRD as illustrated in Fig. 1c. along with the spectrum for $MAPbI_3$ grown on PEDOT: PSS surface under the same processing condition. As a reference, the single crystal $MAPbI_3$ spectrum (taken from reference [45]) is shown in Fig. 1c (black curve) where the diffraction peaks can thus be identified. Deeper analysis of the GIXRD pattern and peak indexing reveals that GIXRD patterns can be identified and properly matched to peaks observed in single crystals of $MAPbI_3$. In addition, various splitting for the typical peaks from the tetragonal phase i.e. (112) and (200) or (004) and (220) as shown in the inset of Fig. 1c, clearly indicate the presence of a stabilized tetragonal phase with enhanced crystallinity. In sharp contrast, the perovskite thin-films fabricated on PEDOT: PSS only exhibit (100) and (200) peaks (cubic phase indexation) and do not exhibit these peak splitting between 20~27 degrees consistent with previous observations using other thin-film processing methods[4,20,48]. To further examine the structure and crystalline quality, we performed a detailed two-dimensional GIWAXS analysis on $MAPbI_3$ thin-films grown on both PEDOT:PSS and LiNiO layers (see Fig. S10 in SI), which is important for understanding the observed peak splitting. The main perovskite peaks can be labeled accordingly on the GIWAXS map consistent with the

https://doi.org/10.1002/adma.201703879
Advanced Materials, 30, 5, 1703879 (2018)

GIXRD spectrums in both of the cases, with typical peaks of the tetragonal phase in the case of LiNiO substrates only. We further did a line-cut analysis in the main (110) peak (Fig. S10 in SI), the $MAPbI_3$ grown on LiNiO shows a peak splitting while the one on PEDOT: PSS only show a merged broad peak. We note that typically in amorphous thin-film the observed splitting of the peaks like in our case is absent because features are often masked due to inhomogeneous peak broadening and as a result most of the weak Bragg reflections disappear. We also conducted a detailed analysis on the diffraction peak FWHM from the GIXRD pattern in Fig. 1c and are summarized in Fig. 1d-e. For the case of $MAPbI_3$ on PEDOT: PSS surface, the XRD peaks are broader for both of the (100) and (200) peaks (cubic phase indexation), thus making it challenging to resolve the weaker reflections. The results of the Integral Breadths (IB) analysis with pseudo-Voigt fits is illustrated in Fig. 1e (the method is described in SI, Equation S1~S5 and Fig. S1). From the peak analysis in Fig. 1e, the correlation lengths are found equal to 48.5 nm for MAPbI3 hot-cast thin-film on LiNiO and 33.9 nm on PEDOT:PSS substrate. Error bars are estimated around 1 nm. More, an additional broadening is related to microstrain distribution in the case of PEDOT: PSS, whereas this distribution is negligible for LiNiO. It clearly implies that the thin film $MAPbI_3$ on LiNiO exhibits enhanced crystallinity by comparison to the sample grown on PEDOT:PSS. This observation is also consistent with the presence of peak splitting characteristic of the tetragonal phase.

Such enhancement in the crystalline quality of $MAPbI_3$ on LiNiO surface is likely due to the different surface nature of LiNiO surface as revealed by the atomic force microscopy images (AFM, Fig. S8) and contact angle measurement (Fig. S9 in SI). The results suggest that LiNiO has crystalline surface with multi-domain that can assist the perovskite nucleation process during film formation[49,50]. In contrast, the PEDOT:PSS surface exhibits amorphous which can impede crystal

https://doi.org/10.1002/adma.201703879
Advanced Materials, 30, 5, 1703879 (2018)

growth. Furthermore, the surface energy of LiNiO is higher than PEDOT:PSS surface as revealed by the contact angle measurement. The LiNiO has higher contact angle when processing with the carrier solvent, leading to a "non-wetting" surface that can assist the crystal formation, which is consistent with literature report [51]. However, we notice that employing room temperature casting method to grow $MAPbI_3$ on the LiNiO surface does not lead to highly crystalline thin film. This suggests that both nucleation site from the surface and processing energy are important during the crystalline film formation.

Moreover, the good match between tetragonal $MAPbI_3$ and LiNiO is further supported using first-principles computational modeling (see Fig 1d, Fig S11 and additional discussion in the SI). Motivated by the superior crystallinity for the thin films of $MAPbI_3$ grown on LiNiO, we fabricated photovoltaic devices to evaluate their optoelectronic properties.

Photovoltaic cell performance

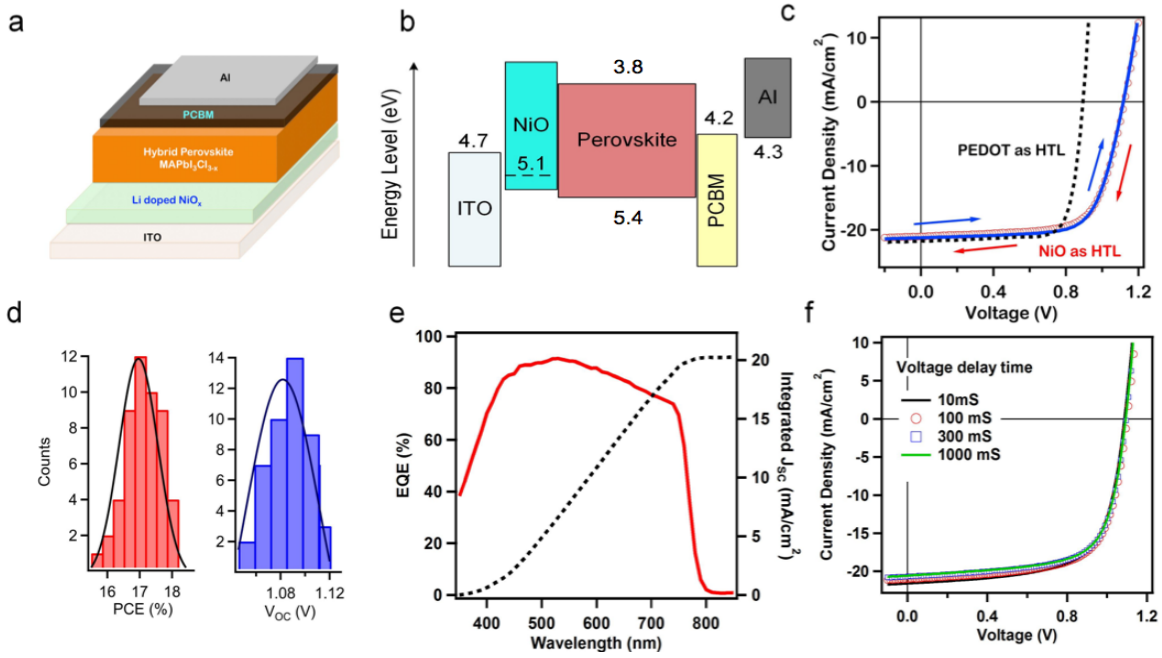

https://doi.org/10.1002/adma.201703879
Advanced Materials, 30, 5, 1703879 (2018)

Figure 2 $MAPbI_3$ Solar cell characteristics using LiNiO as hole transporting layer. a, scheme for planar device structure; **b**, Energy diagram for each layers in the device; **c**, the current-density voltage scan for champion LiNiO device under 1-sun illumination as compared to the PEDOT based device (black dotted line). The hysteresis for LiNiO device is also tested by performing the forward scan (red) and reverse scan (blue) and the two curves overlay on top of each other. **d**, histogram statistical curves for LiNiO device PCE (left) and V_{OC} (right) over 50 device from different batches, **e**, external quantum efficiency (EQE) of the planner solar cell using LiNiO (solid line) and PEDOT (dashed line) as HTL, respectively. **f**, the light J-V curves under 1-Sun for a typical $MAPbI_3$/LiNiO device at different voltage delay time (scan rate).

Figure 2 summarizes the solar cell device structure and performance for the perovskite thin-films on LiNiO as HTL. Figure 2a illustrates the scheme for the planar device structure used in this study (from now on referred to as LiNiO device) along with the energy level alignments of the different layers (Fig. 2b) with respect to the perovskite film derived from previous measurements[52,53]. Here, the LiNiO was spin coated and then sintered (see method section for processing details), followed by hot casting a layer of $MAPbI_3$ of 310±20 nm using our recently published method[42,43,54,55]. PCBM (6,6-phenyl-C61-butyric acid methyl ester) solution was spin coated on top of the hot cast $MAPbI_3$ thin-film to serve as the ETL layer and the device was completed by thermally evaporating aluminum as the cathode. Here the pristine NiO was doped using Li^+ as a dopant to increase the conductivity of the NiO film[56,57] measured by four probe method (see Figure S4 in SI). Figure 2c illustrates the photovoltaic performance obtained by measuring the current density-voltage curve (*J-V*) using an AM 1.5G solar simulator, calibrated using a NIST Silicon photodiode. For our champion LiNiO device, we obtained a V_{OC}~1.12 V with a fill factor of 73.6 % and a short circuit current density (J_{SC}) of 21.79 mA/cm^2, which resulted in a peak power conversion efficiency (PCE) of ~18%. Figure 2d shows the degree of reproducibility captured in a histogram of PCE yielding an average value of 17.0% and V_{OC} of 1.1 V respectively for over 50 LiNiO devices with an active area of 0.5 cm^2. Figure 2e illustrates the external quantum efficiency (EQE) of a typical LiNiO device, which translates to a near equivalent

https://doi.org/10.1002/adma.201703879
Advanced Materials, 30, 5, 1703879 (2018)
short circuit current density (20.23 mA/cm^2) with mismatch of ~7 %. The LiNiO devices exhibit negligible hysteresis in their J-V characteristics as shown in Fig. 2f[6,58].

Spectroscopy characterizations

Next, we investigate photo-physical properties in perovskite thin films grown on LiNiO and directly compare them with that on PEDOT: PSS. We characterize the optical properties of $MAPbI_3$ film grown on LiNiO by photoluminescence (PL) and time-resolved photoluminescence (TRPL) using an excitation energy (wavelength) of 1.80 eV (690 nm). We ensure that the PL signal and TRPL response before and after laser exposure as described in Ref 40 does not change appreciably to affect measurement and the derived conclusions (see detailed method section in SI). The typical absorbance response for $MAPbI_3$/LiNiO sample is plotted in Fig. 3a, which is concomitant with the external quantum efficiency (EQE) measured in Fig. 2e. The PL for $MAPbI_3$ thin films both on LiNiO and PEDOT are shown in Fig. 3a (measured without the electron transporting layer and Al back contact). The optical band-gaps obtained from both the absorption and photoluminescence yield 1.614±0.002 eV (768±1 nm) for $MAPbI_3$/LiNiO, as compared to 1.612±0.002 eV (769±1 nm) for PEDOT: PSS as HTL and the Stokes shift is negligible (<2 meV) in both cases indicating good homogeneity of the perovskite films. Similar value of the optical band-gap for both samples is indicative of the same stoichiometric composition of perovskite as compared to the films on a glass substrate[43].

To quantify the charge recombination processes in both samples, we performed TRPL on $MAPbI_3$ grown on both of the substrates, which monitors the decay of the non-equilibrium carrier density after photo-excitation and relaxation at band edge as described in Fig. 3b, inset. The TRPL data can then be well fitted using the equation:

https://doi.org/10.1002/adma.201703879
Advanced Materials, 30, 5, 1703879 (2018)

where is the bimolecular coefficient, which probes the rate of electron-hole recombination through the band gap, and is the non-radiative decay rate through deep trap[44]. Based on this model, we therefore extracted the and values as a function of excitation intensity as shown in Fig. 3c. From the results, it is clear that both perovskites films grown on LiNiO and PEDOT operate in a regime dominated by bimolecular recombination — the bimolecular coefficients are comparable (Fig. 3c, top panel), of the order of $1.5x10^{-9}$ cm^3/s at solar-equivalent photo-excitation intensity (around 100 mW/cm^2 as highlighted in the figure). However, an important finding is that, we observe a significant reduction of the non-radiative decay rate in the case of $MAPbI_3$/LiNiO (Fig. 3c, bottom panel) in comparison to $MAPbI_3$/PEDOT: PSS samples at low powers. This difference reaches almost one order of magnitude at light intensity equivalent to 1-Sun. The TRPL results indicate that in the operation regime of solar cells, shallow electronic impurity states are passivated, photo-excited carriers undergo a bimolecular recombination process as the main recombination pathway[44]. However, in the case of LiNiO device, photo-excited free carriers have a much lower probability to be quenched by the deeper electronic impurities (Fig. 3b-c) in comparison to the PEDOT: PSS device, especially close to the solar cell operation (~100 mW/cm^2). We attribute such reduced trap assisted recombination to be due to both superior thin-film crystallinity of $MAPbI_3$ grown on LiNiO and the superior quality of the resulting interface possibly due to the passivation effect from the LiNiO interface. Deep level traps are well known to contribute to the overall trap density (bulk and interface) significantly as measured using capacitance and impedance spectroscopy. However, for the $MAPbI_3$ is grown on LiNiO, these trap states are passivated and thus suppresses the non-radiative recombination pathways as revealed using times-resolved photoluminescence experiments described in Fig. 3 and in good agreement with the

https://doi.org/10.1002/adma.201703879
Advanced Materials, 30, 5, 1703879 (2018)

impedance measurement (Fig. S5-6 in SI).

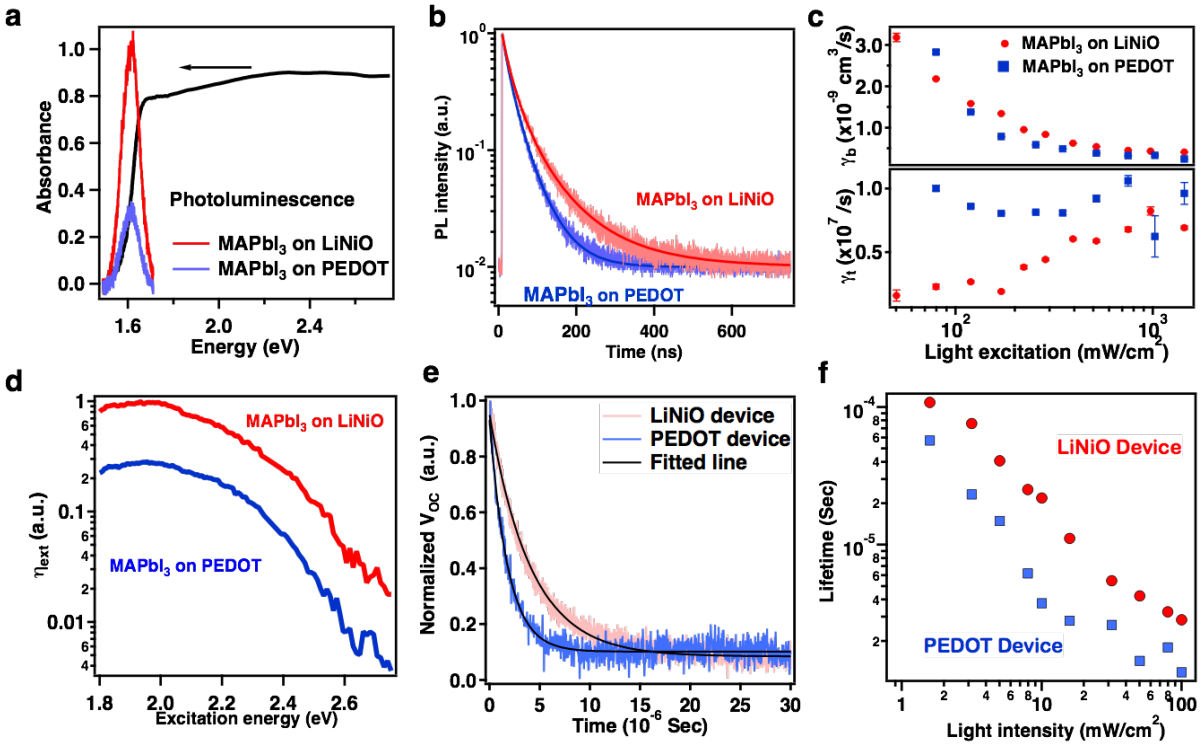

Figure 3 Characterization of non-radiative recombination in the perovskite active layers. a, Optical absorbance for both perovskite thin film devices (blue). Photoluminescence of perovskite thin films on both LiNiO (red) and PEDOT: PSS (black). Color code is kept for the other panels. **b**, Time-correlated single photon counting histograms of the PL (light colors) exciting at 1.80 eV (690 nm) under about 1 sun light intensity and the recombination models (dark colors) for both samples. (inset) Schematics of the modelling of the dynamics of light emission (see text for details). γ_b is the bimolecular coefficient and γ_t the trap-assisted non-radiation relaxation rate. **c,** Bimolecular coefficient (top) and trap-assisted relaxation rate (bottom) as a function of photoexcitation intensity, derived from the fit of the data. The highlighted area represents the 1-Sun equivalent condition. Error bars do not include the maximum 10% error from the absorption. **d**, External photoluminescence efficiency as a function of excitation energy and detecting at 1.62 eV. **e,** Transient photo-voltage (TPV) decay curve under white bias light with intensity equivalent

https://doi.org/10.1002/adma.201703879
Advanced Materials, 30, 5, 1703879 (2018)
to 1-Sun (100 mW/cm^2) generated by LED with small red light perturbation. **f,** Charge recombination lifetime determined by TPV as a function of light intensity for LiNiO (red) and PEDOT (blue) as HTL.

To further understand the origin of the increase in the V_{OC}, we also examine the photoemission properties of the perovskite thin films, in particular, the internal quantum efficiency (η_{int}), and the external quantum efficiency (η_{ext}). Figure 3d shows the relative η_{ext}, *i.e.* the ratio between the photoluminescence intensity and the absorption, as a function of excitation laser energy (see also methods). η_{ext} yields a nearly four-fold increase for $MAPbI_3$ on LiNiO as compared to the $MAPbI_3$ grown on PEDOT. Owing to the reciprocity relationship between open-circuit voltage and external PL efficiency[48] $V_{OC} = V_{OC,\,ideal} - kT\,|\ln(\eta_{ext})|$, an increase of η_{ext} does contribute to the increase of V_{OC} coming from both lowered trap density and fast charge transfer rate. However, a three to four-fold increase in η_{ext} corresponds to a relatively modest contribution to the rise in V_{OC} (~40 meV) as compared to about 200 meV in solar cells. This suggest that the main contribution to the V_{OC} increase in devices with LiNiO as HTL as compared to their PEDOT counterparts, results from a superior quality of the interface with decrease of interface deep-trap states, and better band alignment of the LiNiO Fermi level with the valence band of the perovskites (Fig. 2b) (See supplementary Fig. S7 for detailed discussions).

In summary, our observations in PL and device characterizations support the hypothesis of a smaller density of deep electronic impurities in the bulk and at the perovskite/LiNiO interface. We emphasize from our observations that both the work function alignment with $MAPbI_3$ and the quality of the $MAPbI_3$ thin-film (reduced trap assisted recombination) play a dominant role, which manifests as a large increase in the open circuit voltage.

https://doi.org/10.1002/adma.201703879
Advanced Materials, 30, 5, 1703879 (2018)

Next to explicitly evaluate the quality of the perovskite/HTL interface, we performed transient photo-voltage decay (TPV) measurements (Fig.3, e-f), which gives the rate of recombination of the photo-excited charge at the semiconductor/contact interface during device operation condition. This method has been previously applied to directly prove the quality of the interface in hybrid perovskites and other material systems[59,60]. At open circuit condition, no charges are collected in the outer circuit; the photo-excited excess carriers (minority carrier) generated by the small perturbation under equilibrium charge density produced by white light first reaches the electrode and then recombine near one of the contact interfaces when the light pulse is off, which is observed as a decay in photo-voltage[61]. The lifetime fitted from the decay curve is proportional to the rate of charge recombination near the interface under open circuit condition. Fig. 3e shows a typical TPV decay curve under white light bias for both LiNiO and PEDOT: PSS as HTL. All the curves can be fitted well with a single exponential decay indicating that bimolecular recombination is the dominant process during device operation in both of the devices. This is in agreement with the pure bimolecular process reported above by optical spectroscopy. We further measured the decay curve as a function of background white light bias intensity. The fitted effective-lifetime values are shown in Fig. 3f. As anticipated, the lifetime values for both of the devices decreases with raising light intensity due to increase in the density of photo-generated carriers[62]. By comparing the two devices, for all the light intensities, the LiNiO device has longer recombination lifetime under open circuit condition ranging from 3 μs at 100 mW/cm^2 to 100 μs at 10 mW/cm^2. In contrast, the PEDOT: PSS based device has a much shorter lifetime in the range of 1 μs to 50 μs in the same measurement range. Because the device is fully depleted as revealed using capacitance-voltage measurement, (See supplementary information Fig. S6C), the majority charge is localized near the $MAPbI_3$/contact interface, where carrier recombination is spatially

https://doi.org/10.1002/adma.201703879
Advanced Materials, 30, 5, 1703879 (2018)
most dominant. Therefore the TPV describes the charge recombination through the internal resistor across the two electrodes of the device, the recombination lifetime is thus dominated by the surface recombination[61]. The longer lifetimes in LiNiO device therefore indicate a lower recombination rate compared to the PEDOT: PSS device, which arises from the reduced trap assisted recombination near that interface. The result is consistent with capacitance measurements, which also imply a relatively reduced interface trap density in the case of perovskite/LiNiO. The reduced trap assisted recombination and longer electron lifetime therefore allow the photo-excited charges to be extracted more efficiently before they recombine during device operation, which manifests as a higher open circuit voltage.

Photo Stability

https://doi.org/10.1002/adma.201703879
Advanced Materials, 30, 5, 1703879 (2018)

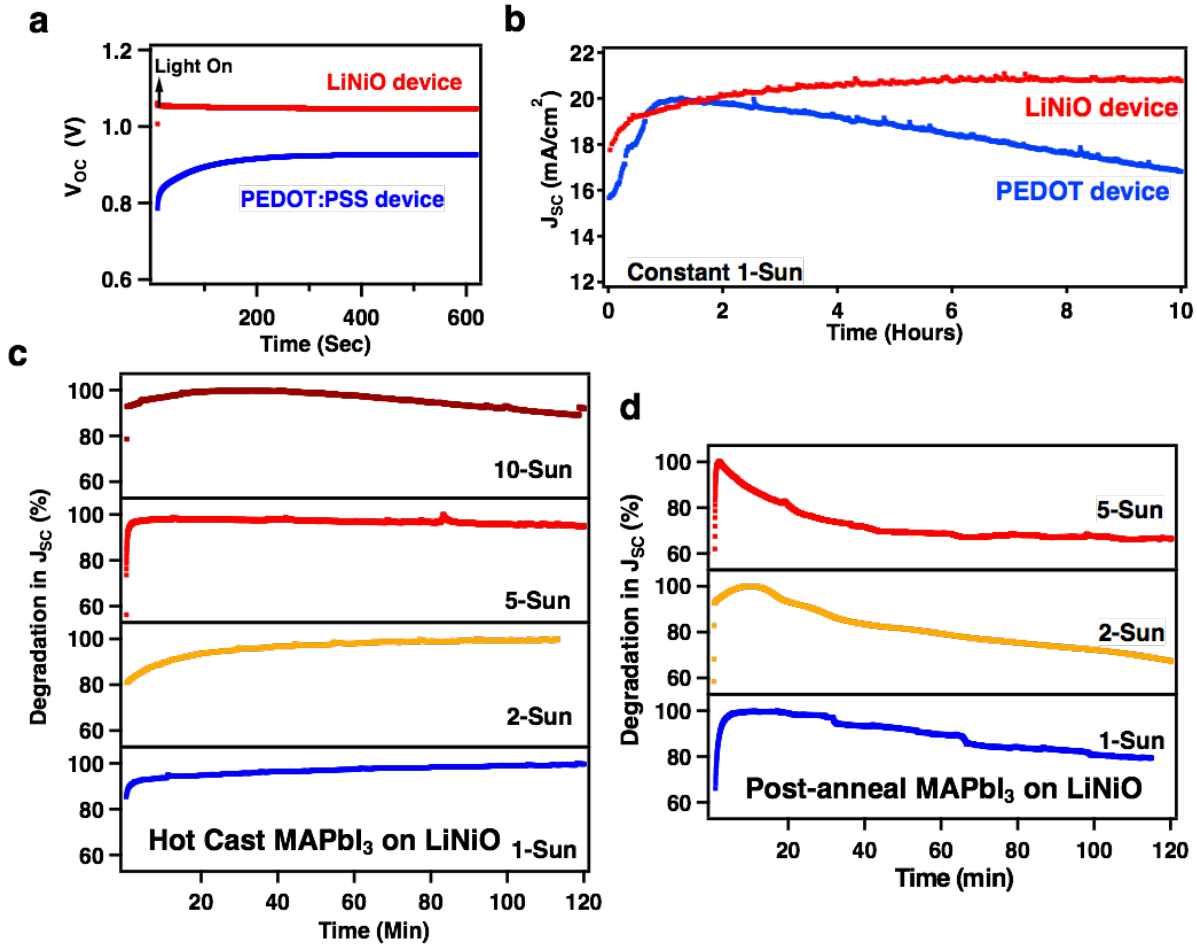

Figure 4. Device stability test under constant illumination with a full spectrum AM1.5G source when mounted under intermediate vacuum. a, Time evolution of V_{OC} after light soaking. **b,** Monitoring the J_{SC} under short circuit condition with AM 1.5G under 1 Sun illumination on PEDOT: PSS and LiNiO devices. J_{SC} time evolution of $MAPbI_3$/LiNiO device growing by **c,** hot-casting method and **d,** post-annealing method under different light intensities.

Finally, in order to evaluate the role of enhanced bulk and interface crystallinity on photo-stability, we performed measurements with continuous light soaking with a full spectrum AM 1.5G source of the perovskite solar cells with LiNiO and compared them to those fabricated using PEDOT: PSS. We recorded the V_{OC} and J_{SC} as a function of illumination time as illustrated in Figure 4. We first look at the V_{OC} and observe that both the devices do not degrade over time with light soaking (Fig. 4a). However, for the PEDOT: PSS based devices, there is a significant increase

https://doi.org/10.1002/adma.201703879
Advanced Materials, 30, 5, 1703879 (2018)
from 0.79V to 0.95 V in the V_{OC} over the first 30 min of light soaking, which has been previously attributed to an initial trap filling[63]. In contrast, such trap filling process is not observed in the LiNiO device and it reaches ~1.1 V almost instantaneously with illumination and thereafter remains flat over the testing period (2 hours), which clearly indicates that the defects at the perovskite/LiNiO are appreciably lower. Next we monitor the changes in the J_{SC} under constant illumination, as illustrated in Fig. 4b. The LiNiO device exhibits excellent stability over 10-hours constant one-sun illumination without additional UV filters. To further evaluate the photocurrent stability, we performed accelerated test by monitoring the J_{SC} under various light intensities, as shown in Fig. 4c. The $MAPbI_3$/LiNiO device shows a stable current output for up to 5-Suns during the testing period. The degradation only sets in after an hour of light soaking at an order of magnitude higher intensities of 10-Suns, most likely due to an increase in temperature[42,44] of the solar cell. In order to compare the perovskite device photo-stability with different degree of crystallinity in the same device configuration, we grow the $MAPbI_3$ thin film using the post-annealing method[64], which leads to a lesser degree of crystallinity (see FWHM comparison in SI, Fig. S12) for detailed structure analysis) on LiNiO HTL. The J_{SC} stability tests under various light intensities are in Fig. 4d. In sharp contrast with the hot-cast films, the device shows significant degradation of J_{SC} starting from 2-Sun illumination.

We recall that the photo-degradation in the J_{SC} was attributed to the formation of light-activated meta-stable trap states (small polarons[65]) and their accumulation in the perovskite layer over several mins to hours, resulting in a slow decrease of photocurrent over time under 1-Sun illumination condition[40]. These light-activated trap states appear as deep-level traps formed by a non-radiative relaxation of photo-excited carriers, leading to the degradation of photocurrent in devices with PEDOT (Fig.4 b,c). They act like “seeds” that with continuous light soaking over

https://doi.org/10.1002/adma.201703879
Advanced Materials, 30, 5, 1703879 (2018)
time lead to the accumulation of trap states and formation of charged regions. Conversely, the improved crystallinity and the strong reduction of deep electronic impurities in perovskite layers on LiNiO prevents generation of such light-activated trap states, while the polycrystalline film produced by post-annealing method still degrades under constant illumination, independent of the HTL layer used in the device (See Fig. S13 in SI).

In summary, through this work we show that improving the crystalline quality of the $MAPbI_3$ material and emergent interface leads to a strong suppression of the deep level defects and leads to much improved charge carrier transport in the bulk and through the interfaces. Altogether, this constitutes an important step towards achieving photo-stable perovskite thin-films not just for photovoltaics but for any conceivable optoelectronic devices.

Discussion

In this study, we report efficient, hysteresis-free and photo-stable hybrid perovskite solar cells enabled by growing highly crystalline $MAPbI_3$ layer using hot-casting on Lithium doped NiO surface. We evaluated the $MAPbI_3$ crystalline structure by GIXRD and microscopy and found a stable tetragonal phase perovskite can be formed on LiNiO. Direct correlations between the degree of crystallinity of perovskite film and improved electronic properties of devices are elucidated via systematic investigations using crystallography, DFT, spectroscopy and device characterizations. In particular, increased V_{OC} in LiNiO devices are found to be directly related with better interface energy level alignment, suppressed trap assisted recombination in the bulk and at the interfacial contacts. Moreover, such devices represent excellent photo-stability under continuous light soaking when exposed to simulated sunlight (AM 1.5G source with no UV filters) and can withstand up to 5-Suns of light intensity. This is a consequence of high degree of thin film

crystallinity and clean interface with reduced trap density on LiNiO surface. As conclusion, we found the structure-property relationships play a crucial role for achieving photo-stable, reliable high efficiency perovskite-based thin-film optoelectronic devices. We anticipate that this work will lead to further efforts on improving the thin film crystallinity as well as interface qualities, and as a result, the overall physical properties. This shall progressively push the field of hybrid perovskites towards the realization of technologically viable stability.

References

1. Lee, M. M., Teuscher, J., Miyasaka, T., Murakami, T. N. & Snaith, H. J. Efficient Hybrid Solar Cells Based on Meso-Superstructured Organometal Halide Perovskites. *Science* **338**, 643 (2012).
2. Burschka, J. *et al.* Sequential deposition as a route to high-performance perovskite-sensitized solar cells. *Nature* **499**, 316-319 (2013).
3. Stoumpos, C. C. *et al.* Crystal Growth of the Perovskite Semiconductor CsPbBr3: A New Material for High-Energy Radiation Detection. *Cryst. Growth Des.* **13**, 2722-2727 (2013).
4. Jeon, N. J. *et al.* Solvent engineering for high-performance inorganic–organic hybrid perovskite solar cells. *Nat. Mater.* **13**, 897-903 (2014).
5. Tan, Z.-K. *et al.* Bright light-emitting diodes based on organometal halide perovskite. *Nat. Nanotechnol.* **9**, 687-692 (2014).
6. Zhou, H. *et al.* Interface engineering of highly efficient perovskite solar cells. *Science* **345**, 542 (2014).
7. Fang, Y., Dong, Q., Shao, Y., Yuan, Y. & Huang, J. Highly narrowband perovskite single-crystal photodetectors enabled by surface-charge recombination. *Nat. Photon.* **9**, 679-686 (2015).
8. Zhu, H. *et al.* Lead halide perovskite nanowire lasers with low lasing thresholds and high quality factors. *Nat. Mater.* **14**, 636-642 (2015).
9. Green, M. A., Emery, K., Hishikawa, Y., Warta, W. & Dunlop, E. D. Solar cell efficiency tables (version 48). *Prog. Photovolt: Res. Appl.* **24**, 905-913 (2016).
10. Saliba, M. *et al.* Cesium-containing triple cation perovskite solar cells: improved stability, reproducibility and high efficiency. *Energy Environ. Sci.* **9**, 1989-1997 (2016).
11. Yang, W. S. *et al.* High-performance photovoltaic perovskite layers fabricated through intramolecular exchange. *Science* **348**, 1234 (2015).
12. Son, D.-Y. *et al.* Self-formed grain boundary healing layer for highly efficient CH3 NH3 PbI3 perovskite solar cells. *Nat. Energy* **1**, 16081 (2016).

13. Bi, C. *et al.* Non-wetting surface-driven high-aspect-ratio crystalline grain growth for efficient hybrid perovskite solar cells. *Nat. Commun.* **6**, 8747 (2015).
14. Li, X. *et al.* A vacuum flash–assisted solution process for high-efficiency large-area perovskite solar cells. *Science* **353**, 58 (2016).
15. Yang, M. *et al.* Facile fabrication of large-grain CH3NH3PbI3-xBrx films for high-efficiency solar cells via CH3NH3Br-selective Ostwald ripening. *Nat. Commun.* **7**, 12305 (2016).
16. Nie, W. *et al.* Interface Design Principles for High-Performance Organic Semiconductor Devices. *Adv. Sci.* **2**, 1500024 (2015).
17. Kim, H.-S. & Park, N.-G. Parameters Affecting I–V Hysteresis of CH3NH3PbI3 Perovskite Solar Cells: Effects of Perovskite Crystal Size and Mesoporous TiO2 Layer. *J. Phys. Chem. Lett.* **5**, 2927-2934 (2014).
18. Shao, Y., Xiao, Z., Bi, C., Yuan, Y. & Huang, J. Origin and elimination of photocurrent hysteresis by fullerene passivation in CH3NH3PbI3 planar heterojunction solar cells. *Nat. Commun.* **5**, 6784 (2014).
19. Tress, W. *et al.* Understanding the rate-dependent J-V hysteresis, slow time component, and aging in CH3NH3PbI3 perovskite solar cells: the role of a compensated electric field. *Energy Environ. Sci.* **8**, 995-1004 (2015).
20. Azpiroz, J. M., Mosconi, E., Bisquert, J. & De Angelis, F. Defect migration in methylammonium lead iodide and its role in perovskite solar cell operation. *Energy Environ. Sci.* **8**, 2118-2127 (2015).
21. Eames, C. *et al.* Ionic transport in hybrid lead iodide perovskite solar cells. *Nat. Commun.* **6**, 8497 (2015).
22. Xu, J. *et al.* Perovskite-fullerene hybrid materials suppress hysteresis in planar diodes. *Nat. Commun.* **6**, 8081 (2015).
23. Zhang, Y. *et al.* Charge selective contacts, mobile ions and anomalous hysteresis in organic-inorganic perovskite solar cells. *Mater. Horiz.* **2**, 315-322 (2015).
24. Yuan, Y. & Huang, J. Ion Migration in Organometal Trihalide Perovskite and Its Impact on Photovoltaic Efficiency and Stability. *Acc. Chem. Res.* **49**, 286-293 (2016).
25. Juarez-Perez, E. J. *et al.* Photoinduced Giant Dielectric Constant in Lead Halide Perovskite Solar Cells. *J. Phys. Chem. Lett.* **5**, 2390-2394 (2014).
26. Hoke, E. T. *et al.* Reversible photo-induced trap formation in mixed-halide hybrid perovskites for photovoltaics. *Chem. Sci.* **6**, 613-617 (2015).
27. Chen, Q. *et al.* Controllable Self-Induced Passivation of Hybrid Lead Iodide Perovskites toward High Performance Solar Cells. *Nano Lett.* **14**, 4158-4163 (2014).
28. Grancini, G. *et al.* Role of microstructure in the electron–hole interaction of hybrid lead halide perovskites. *Nat. Photon.* **9**, 695-701 (2015).
29. Mosconi, E., Meggiolaro, D., Snaith, H. J., Stranks, S. D. & De Angelis, F. Light-induced annihilation of Frenkel defects in organo-lead halide perovskites. *Energy Environ. Sci.*, **9**, 3180-3187 (2016).
30. Kaltenbrunner, M. *et al.* Flexible high power-per-weight perovskite solar cells with chromium oxide-metal contacts for improved stability in air. *Nat. Mater.* **14**, 1032-1039 (2015).

31. Liu, C. *et al.* High Performance Planar Heterojunction Perovskite Solar Cells with Fullerene Derivatives as the Electron Transport Layer. *ACS Appl. Mater. Interfaces* **7**, 1153-1159 (2015).
32. Qiu, W. *et al.* High efficiency perovskite solar cells using a PCBM/ZnO double electron transport layer and a short air-aging step. *Org. Electron.* **26**, 30-35 (2015).
33. Wang, H.-H. *et al.* Improving the TiO2 electron transport layer in perovskite solar cells using acetylacetonate-based additives. *J. Mater. Chem. A* **3**, 9108-9115 (2015).
34. Choi, J., Song, S., Hörantner, M. T., Snaith, H. J. & Park, T. Well-Defined Nanostructured, Single-Crystalline TiO2 Electron Transport Layer for Efficient Planar Perovskite Solar Cells. *ACS Nano* **10**, 6029-6036 (2016).
35. Yang, G., Tao, H., Qin, P., Ke, W. & Fang, G. Recent progress in electron transport layers for efficient perovskite solar cells. *J. Mater. Chem. A* **4**, 3970-3990 (2016).
36. Chen, W. *et al.* Efficient and stable large-area perovskite solar cells with inorganic charge extraction layers. *Science* **350**, 944 (2015).
37. You, J. *et al.* Improved air stability of perovskite solar cells via solution-processed metal oxide transport layers. *Nat. Nanotechnol.* **11**, 75-81 (2016).
38. Kim, J. H. *et al.* High-Performance and Environmentally Stable Planar Heterojunction Perovskite Solar Cells Based on a Solution-Processed Copper-Doped Nickel Oxide Hole-Transporting Layer. *Adv. Mater.* **27**, 695-701 (2015).
39. Tian, Y. *et al.* Giant Photoluminescence Blinking of Perovskite Nanocrystals Reveals Single-Trap Control of Luminescence. *Nano Lett.* **15**, 1603-1608 (2015).
40. Motti, S. G. *et al.* Photoinduced Emissive Trap States in Lead Halide Perovskite Semiconductors. *ACS Energy Lett.*, 726-730 (2016).
41. Yuan, H. *et al.* Photoluminescence Blinking of Single-Crystal Methylammonium Lead Iodide Perovskite Nanorods Induced by Surface Traps. *ACS Omega* **1**, 148-159 (2016).
42. Nie, W. *et al.* Light-activated photocurrent degradation and self-healing in perovskite solar cells. *Nat. Commun.* **7**, 11574 (2016).
43. Nie, W. *et al.* High-efficiency solution-processed perovskite solar cells with millimeter-scale grains. *Science* **347**, 522 (2015).
44. Tsai, H. *et al.* High-efficiency two-dimensional Ruddlesden–Popper perovskite solar cells. *Nature* **536**, 312-316 (2016).
45. Saidaminov, M. I. *et al.* High-quality bulk hybrid perovskite single crystals within minutes by inverse temperature crystallization. *Nat. Commun.* **6**, 7586 (2015).
46. Durand, O., Rogers, D., Teherani, F. H., Andrieux, M. & Modreanu, M. Studies of oxide-based thin-layered heterostructures by X-ray scattering methods. *Thin Solid Films* **515**, 6360-6367 (2007).
47. Halder, N. C. & Wagner, C. N. J. Separation of particle size and lattice strain in integral breadth measurements. *Acta Crystallogr.* **20**, 312-313 (1966).
48. Miller, O. D., Yablonovitch, E. & Kurtz, S. R. Strong Internal and External Luminescence as Solar Cells Approach the Shockley-Queisser Limit. *IEEE J. Photovolt.* **2**, 303-311 (2012).
49. Venables, J. A., Spiller, G. D. T. & Hanbucken, M. Nucleation and growth of thin films. *Rep. Prog. Phys.* **47**, 399 (1984).
50. Wolf, D. E. & Villain, J. Growth with Surface Diffusion. *EPL* **13**, 389 (1990).

51. Bi, C. *et al.* Non-wetting surface-driven high-aspect-ratio crystalline grain growth for efficient hybrid perovskite solar cells. *Nat. Commun.* **6**, 7747 (2015).
52. Irwin, M. D., Buchholz, D. B., Hains, A. W., Chang, R. P. H. & Marks, T. J. p-Type semiconducting nickel oxide as an efficiency-enhancing anode interfacial layer in polymer bulk-heterojunction solar cells. *Proc. Natl. Acad. Sci. U.S.A.* **105**, 2783-2787 (2008).
53. Chueh, C.-C., Li, C.-Z. & Jen, A. K. Y. Recent progress and perspective in solution-processed Interfacial materials for efficient and stable polymer and organometal perovskite solar cells. *Energy Environ. Sci.* **8**, 1160-1189 (2015).
54. Blancon, J.-C. *et al.* The Effects of Electronic Impurities and Electron–Hole Recombination Dynamics on Large-Grain Organic–Inorganic Perovskite Photovoltaic Efficiencies. *Adv. Funct. Mater.* **26**, 4283-4292 (2016).
55. Tsai, H. *et al.* Effect of Precursor Solution Aging on the Crystallinity and Photovoltaic Performance of Perovskite Solar Cells. *Adv. Energy Mater.*,doi:10.1002/aenm.201602159 (2017).
56. Joshi, U. S., Matsumoto, Y., Itaka, K., Sumiya, M. & Koinuma, H. Combinatorial synthesis of Li-doped NiO thin films and their transparent conducting properties. *Appl. Surf. Sci.* **252**, 2524-2528 (2006).
57. Jang, W.-L., Lu, Y.-M., Hwang, W.-S. & Chen, W.-C. Electrical properties of Li-doped NiO films. *J. Eur. Ceram. Soc.* **30**, 503-508 (2010).
58. Snaith, H. J. *et al.* Anomalous Hysteresis in Perovskite Solar Cells. *J. Phys. Chem. Lett.* **5**, 1511-1515 (2014).
59. Knesting, K. M. *et al.* ITO Interface Modifiers Can Improve V_{OC} in Polymer Solar Cells and Suppress Surface Recombination. *J. Phys. Chem. Lett.* **4**, 4038-4044 (2013).
60. Tachan, Z., Hod, I., Shalom, M., Grinis, L. & Zaban, A. The importance of the TiO2/quantum dots interface in the recombination processes of quantum dot sensitized solar cells. *Phys. Chem. Chem. Phys.* **15**, 3841-3845 (2013).
61. Street, R. A. Localized state distribution and its effect on recombination in organic solar cells. *Phys. Rev. B* **84**, 075208 (2011).
62. Maurano, A. *et al.* Recombination Dynamics as a Key Determinant of Open Circuit Voltage in Organic Bulk Heterojunction Solar Cells: A Comparison of Four Different Donor Polymers. *Adv. Mater.* **22**, 4987-4992 (2010).
63. Shao, S. *et al.* Elimination of the light soaking effect and performance enhancement in perovskite solar cells using a fullerene derivative. *Energy Environ. Sci.* **9**, 2444-2452 (2016).
64. Tsai, H. *et al.* Optimizing Composition and Morphology for Large-Grain Perovskite Solar Cells via Chemical Control. *Chem. Mater.* **27**, 5570-5576 (2015).
65. Neukirch, A. J. *et al.* Polaron Stabilization by Cooperative Lattice Distortion and Cation Rotations in Hybrid Perovskite Materials. *Nano Lett.* **16**, 3809-3816 (2016).

Acknowledgements. The work at Los Alamos National Laboratory (LANL) was supported by DoE Office of Basic Energy Sciences Work Proposal 08SPCE973 (W.N., and A.D.M.) and by the LANL LDRD program (A.D.M., A.J.N., and S.T.). This work was done in part at the Center for Integrated Nanotechnologies, an Office of Science User Facility. With help from Dr. Joseph W. Strzalka and use of sector 8-IDE in Advanced Photon Source at Argonne National Laboratory was

https://doi.org/10.1002/adma.201703879
Advanced Materials, 30, 5, 1703879 (2018)
supported by the US Department of Energy, Office of Science, Office of Basic Energy Sciences. The work at ISCR is supported by Agence Nationale pour la Recherche (TRANSHYPERO project). B. T. acknowledges funding from the European Union's Horizon 2020 program, through a FET Open research and innovation action under grant agreement No 687008.

Author contributions. A.D.M. and W.N conceived and designed experiments, co-wrote the MS and analyzed data. W.N. and H.T. fabricated devices, performed the measurements. H.T. took XRD and GIWAX measurements and analyzed data with W.N. J-C.B. performed optical spectroscopy measurements, analyzed the data under the supervision of J.C. C.C, and M.G. K. did the crystallography analysis. B. T. performed the DFT computations under the guidance of M. K. and C. K. J. E. and C. K. participated to analyze the data. All authors participated manuscript writing and discussion.

Competing financial interests. The authors declare no competing financial interests for this work

Materials & Correspondence. Correspondence and request for materials should be addressed to wanyi@lanl.gov and amohite@lanl.gov.

Supplementary information for

Contents

https://doi.org/10.1002/adma.201703879
Advanced Materials, 30, 5, 1703879 (2018)

Methods

LiNiO solution preparation: LiNiO solution was prepared according to literature, by dissolving 0.1M Nickel (II) acetate tetrahydrate (99.998%, Sigma-Aldrich) in absolute ethanol (Sigma-Aldrich) with Monoethanolamine (MEA). The molar ratio of Ni^{2+} and MEA is kept to be 1:1. After the solution was stirred at 60 ºC for 1 hour, a clear and deep green solution was formed. The lithium nitrate was added at X molar % (X=0, 2, 5, 10, 20) was added as Li^{+} source to improve the conductivity of the NiO film.

Perovskite solution: the $MAPbI_3$ precursor was prepared by dissolving lead iodide (PbI_2) and Methylammonium iodide (99.8% Sigma-Aldrich) and Methylammonium chloride (molar ratio =1:0.5:0.5) in anhydrous N, N-Dimethylformamide (DMF) with molar concentration of 0.43M. The prepared solution was stirred for at least 24 hours at 70 ºC before using.

Device fabrication: The patterned fluorine doped Tin Oxide (FTO, Thin Film Device Inc) slides were first cleaned in ultra-sonication bath in water, acetone and isopropyl alcohol for 15 min respectively. The substrates were then dried under nitrogen air flow followed by 30 min baking on hot-plate in air for 30 min. The dried substrates were treated by oxygen plasma for 3 min before coating. The in stock solution of LiNiO precursor or PEDOT: PSS (Clevis 4083) were coated by spin coating at 3000 rpm and 5000 rpm respectively for 40 Sec to serve as hole transporting layer (HTL). The substrates were dried at 150 ºC for 20 min in the air. The LiNiO/FTO substrates were then taken into a tube furnace for 450 ºC sintering in ambient condition. The coated substrates were then transferred into an argon filled glovebox for perovskite and top contact deposition. The $MAPbI_3$ layers were produced by hot casting method, where the LiNiO or PEDOT: PSS coated

https://doi.org/10.1002/adma.201703879
Advanced Materials, 30, 5, 1703879 (2018)
substrates were first heated at 150 ºC and then quickly transferred to the spin coator chunk and spinning process was started immediately after dropping the precursor on the substrates at 5000 rpm without ramping for 20 Sec. The film color changed from transparent to dark brown almost instantaneously after solvent escaped. The obtained $MAPbI_3$ on HTL/FTO substrates were then loaded into a vacuum chamber for aluminum deposition after coating by PCBM solution as electron transporting layer.

Solar cell characterization:

The solar cells were characterized by taking current-voltage curves under solar simulator with light intensity equivalent to 1-Sun (100 mW/cm^2) with air mass 1.5 G filter. The devices were masked to reduce error induced edge effect. The external quantum efficiencies were collected by illuminating the device under monochromatic light using a tungsten source (chopped at 150 Hz) while collecting the photocurrent by lock-in amplifier in AC mode. The light source spectrum response was characterized by calibrated silicon diode (FDS1010, Thorlab).

Transient photo-voltage (TPV) measurement: The device was connected to 5 Mohm resistor to be maintained under open circuit condition. TPV data were obtained by measuring the voltage drop at the resistor and the decay curve was recorded by oscilloscope after a small AC red light perturbation ($\Delta V<20$ mV) and under a DC white LED background ($V_{OC}>500$ mV)[1,2]. The white LED light power was maintained at equivalent to 1-Sun by matching the device short circuit current density taken under solar simulator. The light intensity was further changed by inserting a neutral density filter.

https://doi.org/10.1002/adma.201703879
Advanced Materials, 30, 5, 1703879 (2018)

Impedance spectroscopy

The impedance spectroscopy on the device was performed by measuring the device depletion capacitance while applying a small perturbation AC field (V_{ac}=20 mV) superimposed on top of a DC field across the two electrodes of the cell. All the measurements were carried out in dark. By changing the AC field frequency while fixing the AC field amplitude at 20 mV and DC field to be 0, the capacitance as a function of frequency spectrum was extracted. While fixing the frequency and the V_{ac}, and varying the DC field across the device, the capacitance-voltage curve was measured.

Photoluminescence characterization

Optical absorption, photoluminescence (PL), time-resolved photoluminescence (TRPL)

PL, TRPL and optical absorption were performed with a home built confocal microscopy system focusing a monochromatic 6-ps-pulsed laser (repetition rate between 1 MHz) close to the diffraction limit. PL, reflection, and transmission spectral responses were obtained through a spectrograph (Spectra-Pro 2300i) and a CCD camera (EMCCD 1024B) yielding a maximum error of 2 nm. PL data in the main text were measured for light excitation at 690 nm (1.80 eV) and the excitation intensity was typically chosen to be equivalent to 1-Sun (~ 100 mW/cm^2) unless otherwise noted.

TRPL measurements were performed by means of a time correlated single photon counting module (PicoHarp 300) combined with an Avalanche Photo-Diode (MPD-SPAD) through a spectrograph to remove all laser light excitation.

Samples were measured under vacuum (10^{-5}-10^{-6} Torr) under room temperature if not mentioned otherwise.

https://doi.org/10.1002/adma.201703879
Advanced Materials, 30, 5, 1703879 (2018)

Absolute absorption and photoluminescence quantum yield (PLQY)

Absolute absorption and PLQY of the thin films were measured by means of an integrating sphere, following ref. (*28*), in air under ambient conditions. Measurements were acquired directly after taking the samples out of vacuum to minimize effects of air exposure, and some of the samples were encapsulated for cross-check of the data. Alternatively, we performed these measurements in the microscope and verified a meaningful set of data points using the integrating sphere.

DFT simulations:

The calculations were performed within the Density Functional Theory (DFT)[3,4] as implemented in SIESTA package[5] with a basis set of finite-range of numerical atomic orbitals. We used the van der Waals density functional with C09 exchange[6] to describe the exchange-correlation term. This functional has proven to provide superior description of experimental lattice constants similar to those obtained with the optimized GGA based PBEsol functional[7]. Norm-conserving Troullier-Martins pseudopotentials were used for each atomic species to account for the core electrons [8]. $1s^1$, $2s^22p^2$, $2s^22p^3$, $5s^25p^5$, $5d^{10}6s^26p^2$, $2s^22p^4$ and $4s^23d^8$ were used as valence electrons for H, C, N, I, Pb, O and Ni respectively. Polarized Double-Zeta (DZP) basis set with an energy shift of 200 meV were used for the calculations. For the real space mesh grids, energy cutoffs of 200 and at least 500 Rydberg were respectively used for $MAPbI_3$ bulk and systems including NiO (bulk NiO and interfaces with NiO).

For the bulk $MAPbI_3$ and NiO crystals, and the $MAPbI_3$/NiO interfaces, the Brillouin zone was sampled with 4x4x4, 6x6x6 and 4x4x1 Monckhorst-Pack grids, respectively. An effective Hubbard parameter U of 6.0 eV has been applied to Ni d-states according to Dudarev et al.[9]

https://doi.org/10.1002/adma.201703879
Advanced Materials, 30, 5, 1703879 (2018)

Integral Breadths (IB) analysis with pseudo-Voigt fits of the GIXRD pattern

In powder diffraction, line profile analysis of the Bragg-Brentano diffraction peaks is a well-known method to obtain a measure of the coherent-correlation lengths and to characterize the micro-strains distribution. Among these techniques, the integral-breadth (IB) method, using the simulation of the diffraction line-profile, mostly using Voigt functions or pseudo-Voigt functions, provides a rapid and convenient measure of both these parameters. The line broadening is characterized to the correlation length L and to the micro-strain parameter ε. It is therefore possible to obtain both parameters by merely using, respectively, the relations of Scherrer [10,11] or of Stockes and Wilson [12]:

$$L = \frac{K\lambda}{\beta_L(2\theta)\cos\theta_B} \qquad \text{(S1)}$$

$$\varepsilon = \frac{1}{4}\beta_\varepsilon(2\theta)\cot an\theta_B \qquad \text{(S2)}$$

Where θ is the Bragg peak position $\beta_L(2\theta)$ is the integral breadth of the diffraction peak due to a loss of diffraction coherence and $\beta_\varepsilon(2\theta)$ is the integral breadth of the diffraction peak due to a broadening from micro-strains, into scale of the 2θ variable. K is the Scherrer constant fixed at 0.9 in the following. These integral breadths have been turned into scale of the variable $S = \frac{2\sin\theta}{\lambda}$ by the well-known following relationship:

$$\beta(S) = \beta(2\theta)\ \frac{\cos\theta}{\lambda} \qquad \text{(S3)}$$

https://doi.org/10.1002/adma.201703879
Advanced Materials, 30, 5, 1703879 (2018)

The separation of both strain and correlation effects in the IB measurements can be done.. In the past, approximate methods have usually involved the assumption that the constituent profiles are either Cauchy or Gaussian (Williamson–Hall plots). Schoening[13] and Halder and Wagner[14] have shown that the correlation contribution is approximatively described by a Cauchy (Lorentzian) function and the strain one is represented by a Gaussian function. Therefore, a better representation of the experimental profile is given either by a convolution of these functions[15,16] (Voigt functions) or by a linear combination of these functions (pseudo-Voigt functions)[17]. Halder and Wagner[14] have developed the approximate equation to separate both the effects:

$$\beta^2(s) = \beta_{Cauchy}(S).\beta(s) + \beta_{Gauss}{}^2(S) \qquad \text{(S4)}$$

with ***β(S)*** the measured IB. This gives, using Eqs. (1) and (2), the correlation length and the micro-strain parameter. Eq. (4) can be written as follows, using Eqs. (1) (2) and (3):

$$\left(\frac{\beta(s)}{S}\right)^2 = 4\varepsilon^2 + \frac{0.9}{L}\frac{\beta(s)}{S^2} \qquad \text{(S5)}$$

Therefore, the slope of $\left(\frac{\beta(s)}{S}\right)^2$ as a function of $\frac{\beta(s)}{S^2}$ yields L[18]and the origin of the curve ε. This plot is called "Halder–Wagner plot" (a kind of modified "Williamson–Hall" plot).

https://doi.org/10.1002/adma.201703879
Advanced Materials, 30, 5, 1703879 (2018)

Film morphology characterization

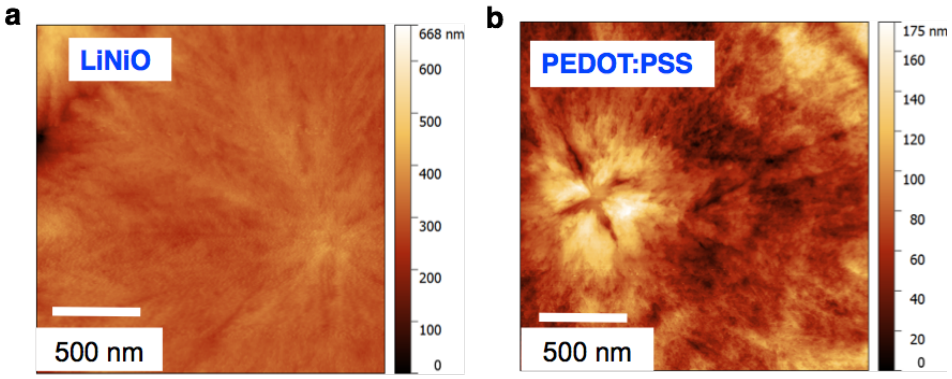

Figure S1. AFM images of $MAPbI_3$ grown on LiNiO and PEDOT:PSS (a, b).

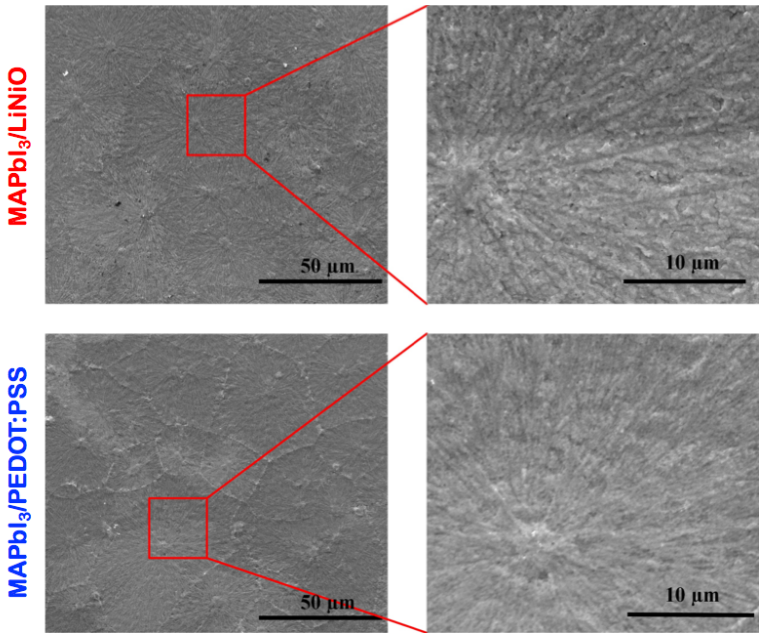

Figure S2. Scanning electron microscopy images for $MAPbI_3$ coated on LiNiO (upper row) and on PEDOT:PSS (lower row) with 2000 and 10000 magnifications. Both $MAPbI_3$ films are processed under the same hot-casting conditions from the same precursors.

The films were deposited under identical conditions using the hot-casting method. Such method leads to large grain feature on the surface of the film as observed in the zoomed-out images and "leaf-like" micron structures in the zoomed in version of the surface. As it can be observed from the SEM images, the morphologies are quite similar.

https://doi.org/10.1002/adma.201703879
Advanced Materials, 30, 5, 1703879 (2018)

Effect of Lithium dopant in NiO

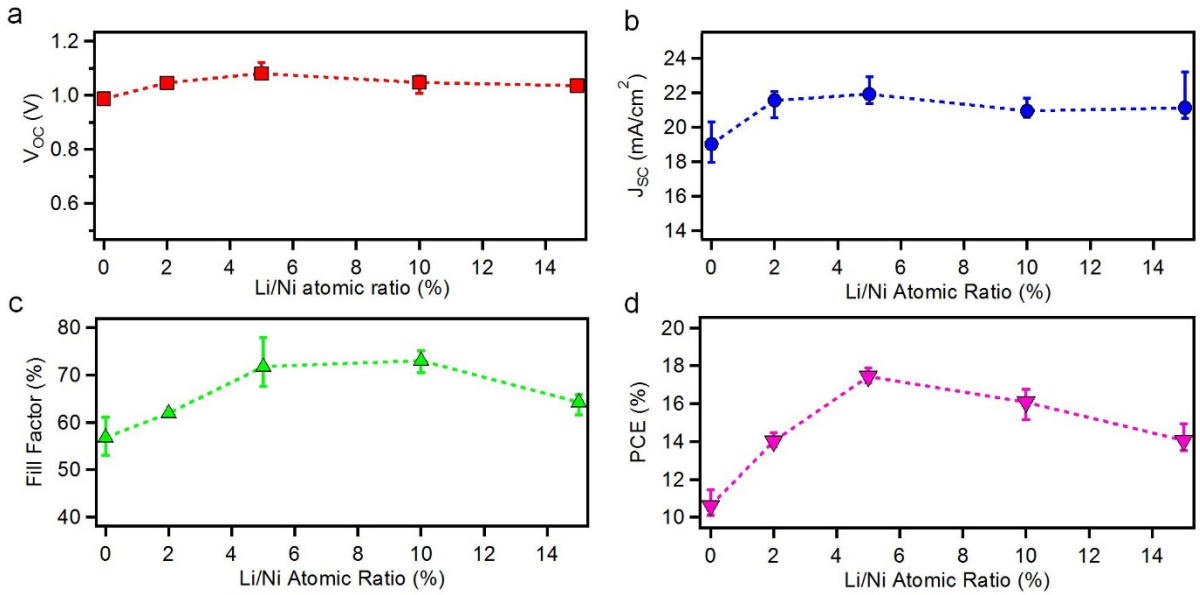

Figure S3. Effect of Li dopant in LiNiO to the solar cell performance evaluated by J-V characteristics under 1-Sun illumination. The Figure shows the figure of merit of solar cell performance extracted by light J-V curves.

NiO is known to be less conductive due to the relatively low carrier density. We therefore doped the NiO thin film by Lithium as suggested by literature. The solar cells performance as a function of Li dopant (by atomic percent) are shown in Figure S3. It is clear that by adding a small amount of Li doping (5 %~10 %), the performance was improved by 40 % because of the increase in J_{SC} and FF.

https://doi.org/10.1002/adma.201703879
Advanced Materials, 30, 5, 1703879 (2018)

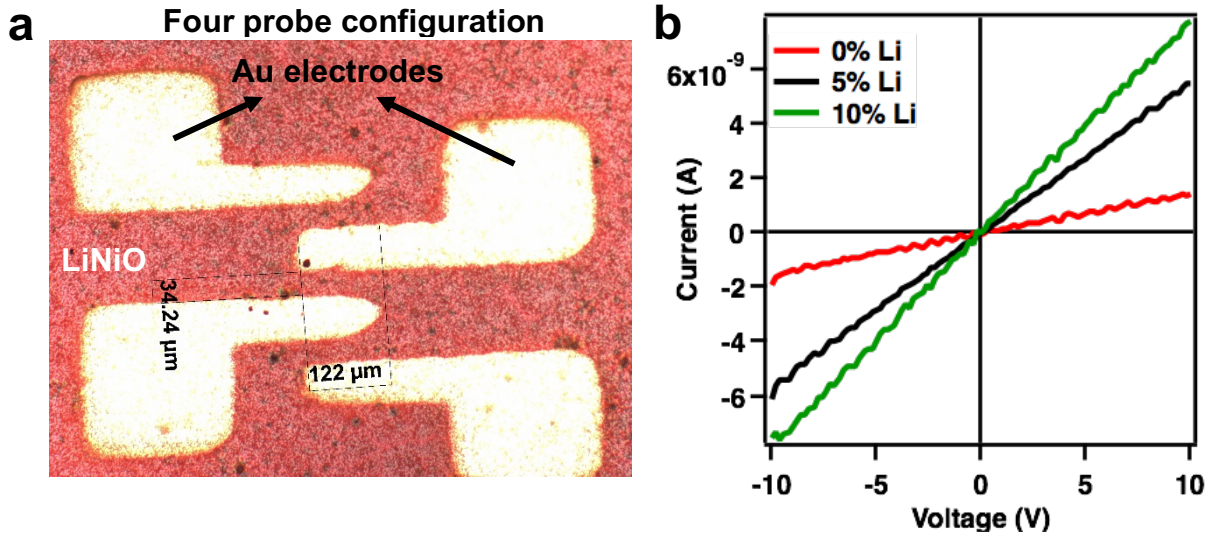

Figure S4. Four probe conductivity measurement for LiNiO thin films spin coated on glass substrates. a, device configuration for four probe measurement used in this study. b, current-voltage curve of LiNiO thin film measured on the device shown in a. The voltage was applied between two middle electrodes and current was collected from the two outer electrodes.

To further characterize the effect of Li doping in NiO film, we performed the thin film conductivity measurement using four probe method as illustrated in Figure S4. The LiNiO films were spin coated on glass substrates and gold electrodes were deposited by thermal evaporation through a shadow mask and were aligned in a line shape. The current-voltage curves are shown in Figure S4b. It is clear that by doping with Lithium, the NiO thin film conductivity increase by 3 folds, which is the major reason for the observed increase in J_{SC} and FF.

Capacitance voltage measurement

https://doi.org/10.1002/adma.201703879
Advanced Materials, 30, 5, 1703879 (2018)

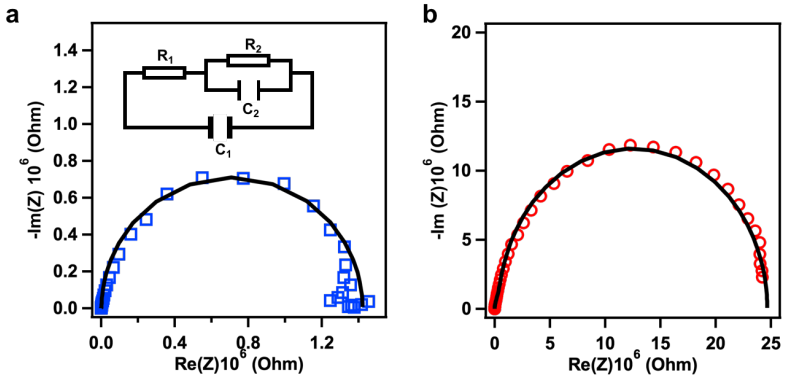

Figure S5. Impedance data for a, PEDOT and b, LiNiO based devices. Symbols are experimental data and solid line is the fitting curve. The equivalent circuit for the fitting is shown in the inset of a.

We employed a commonly used equivalent circuit model as shown in Figure S5. The semicircles for both devices can be fitted by a simple RC circuit at the frequency range of 10~10^4 Hz as described by the equivalent circuit in Figure S5a inset. In the model, the R1||C1 circuit represents the transport resistance and geometric capacitance of the device, which is related to the high frequency data points. The main circle shown in the plots can be fitted by R2||C2 near 10^4~1 Hz range, which is attributed to the interface response of the device. This is consistent with the discussion in the supplementary information for Fig S6, the phase angle for the device in the frequency range near ~10^3-10^4 Hz is close to 90°, which indicates such frequency range is a typical RC circuit response and can be modeled by the trap state response near the interface.

https://doi.org/10.1002/adma.201703879
Advanced Materials, 30, 5, 1703879 (2018)

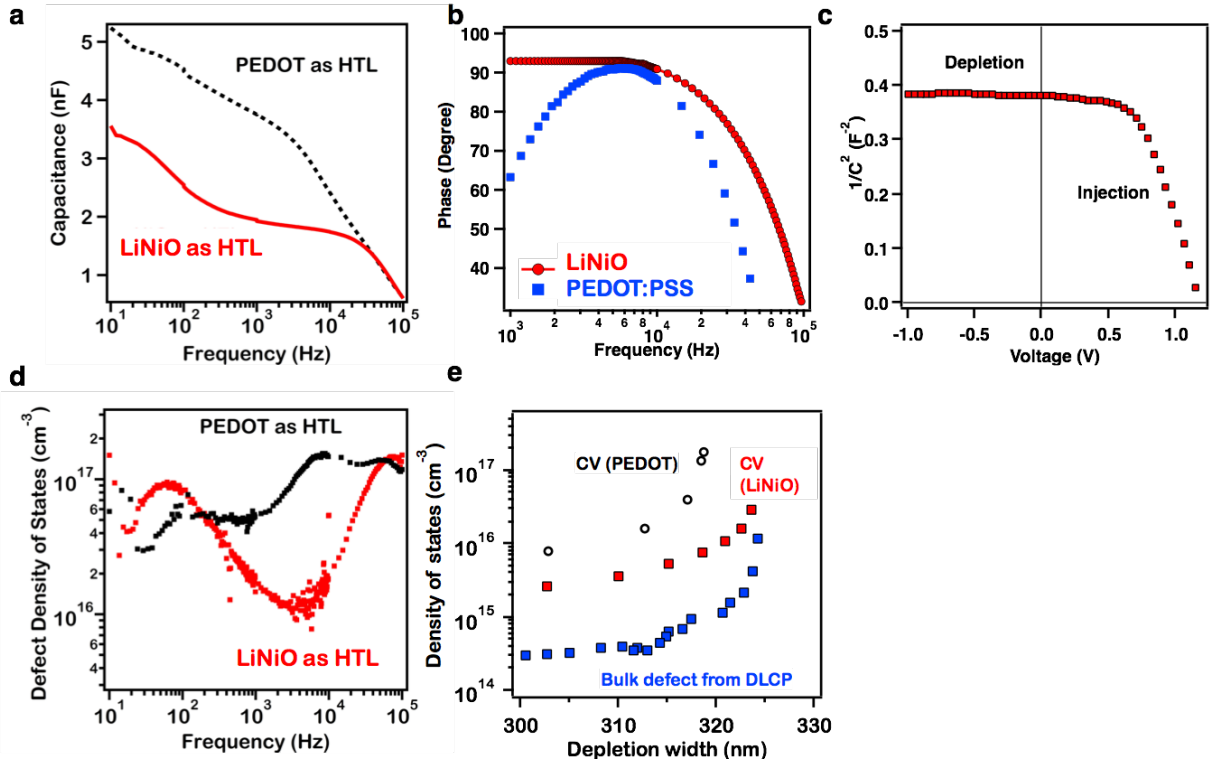

Figure S6 Impedance spectroscopy characterization for $MAPbI_3$ device using LiNiO and PEDOT: PSS as HTL. a, capacitance as a function of frequency spectrum. b, phase angle as a function of frequency. c, capacitance-voltage curve plotted according to Mott-Schottky relation for the LiNiO device. d, defect density of states calculated from a. e, defect density of states measured by capacitance-voltage curve near the depletion region edge for LiNiO and PEDOT: PSS. The bulk defect density is obtained by measuring the non-linear capacitance using drive level capacitance profiling method.

We performed impedance spectroscopy (capacitance-frequency and capacitance voltage measurements) on the LiNiO devices and compared them with PEDOT:PSS devices with the same perovskite film thickness. The results are illustrated in Figure S6. First we measure the capacitance as a function of AC field frequency (V_{ac}=20 mV) with no DC field (See Fig. S6a). The phase angle is also evaluated in Figure S6b. From these results, both the LiNiO and PEDOT:PSS based devices can be fitted with a simple R-C circuit in the frequency window of 10^3~10^4 Hz[19] (see Fig. S5 and related discussion). The trap density of states can thus be extracted from the capacitance-frequency spectrum[19,20]. By taking the 1st order derivative of the capacitance (Fig. S6a), one can obtain the

https://doi.org/10.1002/adma.201703879
Advanced Materials, 30, 5, 1703879 (2018)
trap density of states at different frequencies[21,22] shown in Figure S6d. In the LiNiO device, there is a peak near 10^5 in the measurement window, which represents a shallow trap states. However, in the PEDOT: PSS device, two peaks are observed near 10^4 Hz and 10^5 Hz. The major difference in defect density in LiNiO based device is the two-orders lower trap density (8×10^{15} cm^{-3}) near 10 kHz as opposed to 2×10^{17} cm^{-3} for the PEDOT: PSS device.

We further explore the trap states spatial distribution profile by capacitance-voltage (C-V) and drive level capacitance profiling (DLCP) at this frequency (10^4 Hz) which gives the biggest difference in those two devices. First by looking at the standard C-V measurement for the LiNiO device in Figure S6c, the slope near -1-0 V is nearly flat indicating the device is fully depleted. This is expected for $MAPbI_3$ device acting like a P-I-N type of diode without ionic vacancy that generally can be detected as charge distribution in the intrinsic layer. This is a result of the high quality thin film produced from hot-cast method without ionic vacancies or shunt in the film as also evidenced by the cross-section SEM image in Figure 1-a,b in the MS.

Next we performed a previously developed DLCP measurement, which measures the depletion non-linear capacitance by varying the AC field amplitude at fixed band bending condition ($V_{AC}+V_{DC}$=constant). The calculated trap density is the true bulk density from the depletion region without the influence of the deep level defects from interface[23,24]. The calculated trap density as a function of distance from the center of the device is shown in Figure S6e. It is clear that the bulk trap states (N_{DLCP}) at 10 kHz is in the order of 10^{14}~10^{15} cm^{-3} in the depletion region for LiNiO based devices, which is in the same order of magnitude of the results obtained for PEDOT device. However, the trap density calculated from standard C-V (N_{CV}) for the PEDOT based device is 10^{16}~10^{17} cm^{-3}, which indicates that PEDOT: PSS devices are strongly influenced by the interface deep trap states giving rise to a high value in N_{CV}. However, the N_{CV} value for

https://doi.org/10.1002/adma.201703879
Advanced Materials, 30, 5, 1703879 (2018)

LiNiO device is calculated to be 10^{15}~10^{16} cm^{-3}, which is much closer to the N_{DLCP}, indicating in this case the interface states are significantly reduced.

Optical spectroscopy measurement

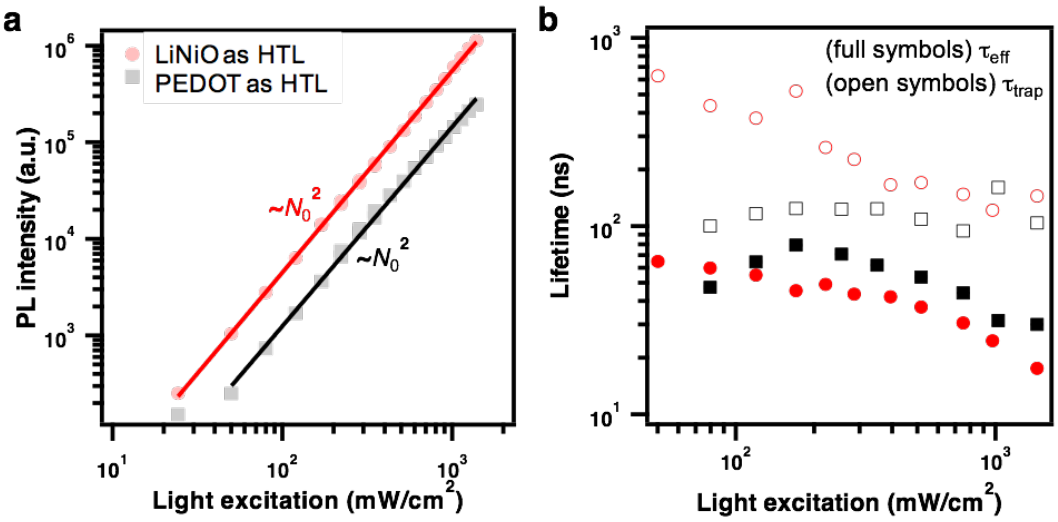

Figure S7 Optical spectroscopy on $MAPbI_3$ on LiNiO (circles) as compare to that on PEDOT: PSS (squares). a, PL intensity as a function of excitation power. b, effective lifetime value extracted from the TRPL from bimolecular recombination (full symbols) and trap assisted recombination (open symbols).

Figure S7a shows the PL intensity as a function of excitation power for $MAPbI_3$ both on LiNiO and PEDOT: PSS substrate. The PL signal follows the square of the photo-excitation intensity, which is indicative of free carrier recombination[25] intrinsic to the $MAPbI_3$ thin-film, independent of the HTL layer.

The effective lifetime value for charge carriers that recombine through bimolecular process and trap assisted process are shown in Figure S7b. The effective lifetime was extracted according to the model mentioned in the manuscript (Fig. 3b and related discussion), from which we extracted the and values as a function of excitation intensity as shown in Figure 3c, and subsequently the effective recombination lifetimes through bimolecular process () and through trap

https://doi.org/10.1002/adma.201703879
Advanced Materials, 30, 5, 1703879 (2018)
() shown in Figure S7b. The model yields excellent fits (with R^2 coefficients exceeding 0.998) to the TRPL responses in both of the samples. In the case of perovskite on LiNiO, the majority of free carriers decay via bimolecular recombination with = $1.6x10^{-9}$ cm^3/s with negligible non-radiative decay process; in fact, the effective lifetime of carriers that undergo bimolecular recombination τ_{eff}[26] is almost one order of magnitude smaller than the trap-assisted non-radiative decay lifetime τ_{trap}, *i.e.* ns and ns at about 100 mW/cm^2. Using a typical mobility of about 5 cm^2 V^{-1} s^{-1} in our solar cells corresponding to a Langevin bimolecular coefficient cm^3 s^{-1}, we find that , which evidences that our devices operate in the non-Langevin regime; in agreement with previous reports[25]. This is a necessary condition to achieve good carrier extraction and high performance in low mobility semiconductor solar cells[27].

Possible mechanism for perovskite thin film growth on LiNiO

To propose a possible mechanism for perovskite thin film growth on the different substrates, we have *(i)* explored the surface properties of those substrates (surface morphology and surface energy by atomic force microscopy and contact angle techniques), *(ii)* further examined the structure and crystal quality (GIWAXS analysis) and *(iii)* theoretically investigated the MAPbI3/NiO interface (DFT calculations).

1. Surface morphology

We studied the surface roughness of the LiNiO substrate by atomic force microscopy measurement. In comparison, we have done the AFM on PEDOT:PSS surface. The results are shown in Figure S8.

https://doi.org/10.1002/adma.201703879
Advanced Materials, 30, 5, 1703879 (2018)

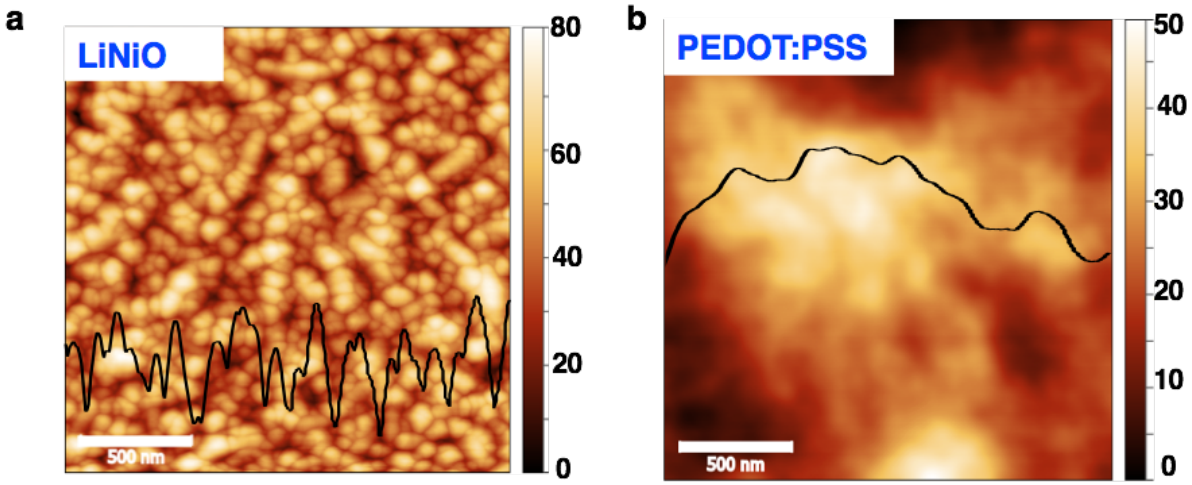

Figure S8. Atomic force microscopy images for a, LiNiO and b, PEDOT:PSS coated on FTO substrate

From the results, we found the surface of LiNiO has higher roughness value ~32nm ± 12nm (RMS= 11.95nm) while the PEDOT: PSS surface is much smoother with with 20nm ± 5nm (RMS = 9.61nm). Furthermore, the LiNiO surface shows multiple crystalline domains with size in the order of 10th of nanometers. This is a result of the crystalline thin film formation by high temperature post-annealing (~450ºC). On contrary, the PEDOT: PSS surface is more amorphous without any clear signature of crystalline domain, which is a typical polymer surface processed from solution. According to the surface morphology difference, it suggests that the LiNiO surface provides better crystal formation environment because of the large surface roughness with multiple nano-size crystalline domains, that serves as nucleation sites that assist perovskite crystal formation thus leading to a highly crystalline perovskite thin film.

2. Surface energy by contact angle measurement

We further explored the surface interaction energy between the LiNiO and the processing solvent (Dimethyl sulfoxide, DMSO) by contact angle measurement, as shown in Figure S9. The PEDOT: PSS surface was also explored for comparison. The contact angle for DMSO on LiNiO surface is

https://doi.org/10.1002/adma.201703879
Advanced Materials, 30, 5, 1703879 (2018)

measured to be 31º±2º. This means the wetting of DMSO is good enough for thin film formation. However, it is much higher than the case of PEDOT: PSS surface on which DMSO wets the surface very well (~7.4º±1º).

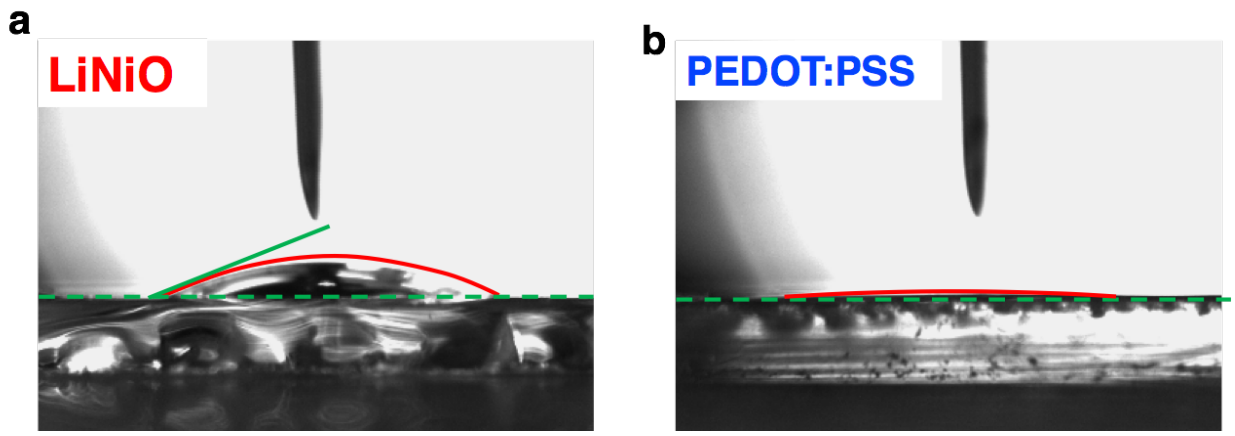

Figure S9. Contact angle using DMSO as probing solvent for (a) LiNiO surface as compared to (b) PEDOT:PSS surface.

According to the work by Bi et al[28], a non-wetting surface will enhance hybrid perovskite grain formation. This is because of increased nucleation spacing between solution droplet and low surface tension dragging force, which increase grain boundary mobility and allow the crystalline film to grow in larger degree of freedom. Based on the report and contact angle results, it clearly indicates that larger surface energy (with respect to the processing solvent) on LiNiO case also allows larger degree of freedom for the crystal grain growth and thus leading to a compact and highly crystalline thin film.

3. GIWAXS line cuts

To further examine the structure and crystalline quality, we performed a detailed two-dimensional GIWAXS analysis on $MAPbI_3$ thin-films grown on both PEDOT:PSS and LiNiO

https://doi.org/10.1002/adma.201703879
Advanced Materials, 30, 5, 1703879 (2018)

layers (Fig. S10). The GIWAXS line cuts for perovskite thin-films fabricated on LiNiO allow peak indexing similar to the one made in Figure 1c from the GIXRD spectra (Fig. S10a), with well-resolved peak splittings. Contrarily, the (112) and (200) splitting can hardly be resolved in the GIWAXS map for $MAPbI_3$ grown on PEDOT: PSS (Fig. S10b).

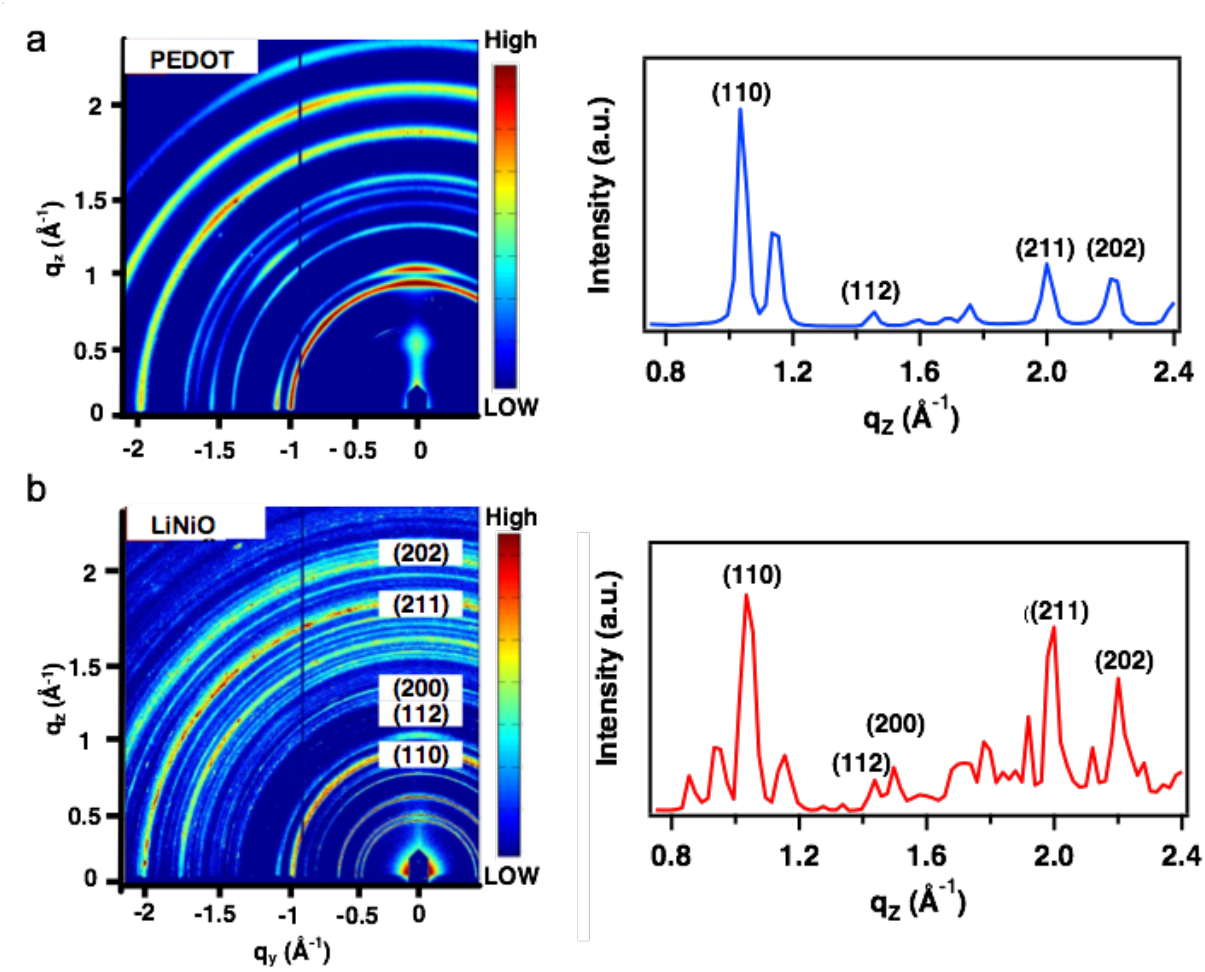

Figure S10. GIWAXS map for $MAPbI_3$ grown on a, LiNiO substrate and b, PEDOT:PSS substrates with line cut along the q_z direction respectively.

4. $MAPbI_3$/NiO model interface by first principles

We started with the orthorhombic crystal structure of $MAPbI_3$ where the MA molecules have a well-defined position within the inorganic Pnma lattice. Considering the experimentally

https://doi.org/10.1002/adma.201703879
Advanced Materials, 30, 5, 1703879 (2018)

observed (001) surface of NiO[29,30], and corresponding lattice parameters, $MAPbI_3$ appears to afford appropriate lattice matching for a $MAPbI_3$/NiO interface (Tables S1-S2).

Table S1. Lattice constants of bulk NiO, $MAPbI_3$.

	a (Å)		**b** (Å)		**c** (Å)	
	exp.	calc.	exp.	calc.	exp.	calc.
NiO bulk	4.17[31]	4.25	4.17[31]	4.25	4.17[31]	4.25
$MAPbI_3$ bulk	8.84[32]	8.74	12.58[32]	12.58	8.56[32]	8.40

Table S2. Lattice mismatch of the $MAPbI_3$/NiO model interface. The stacking axis is chosen as the $\mathbf{c}_i$ axis, ($\mathbf{a}_i$,$\mathbf{b}_i$) defining the in-plane crystallographic axes. $\mathbf{a}_i$ = **a**(NiO) = **c**($MAPbI_3$) and $\mathbf{b}_i$ = **b**(NiO) = **a**($MAPbI_3$).

direction	$\mathbf{a}_i$	$\mathbf{b}_i$
lateral mismatch of $MAPbI_3$ on NiO (%)	**-1.18%**	**2.82%**

NiO crystallizes in the rock-salt (NaCl) cubic lattice with Fm-3m space group at room temperature and exhibits an antiferromagnetic ordering with ferromagnetic sheets of (111) planes alternating anti-ferromagnetically along the [111] direction[29,33]. Moreover, the measured (100) surface of NiO also has an antiferromagnetic ordering[29,30]. Hence, we consider NiO in its anti-ferromagnetic spin configuration for both its bulk structure and within the $MAPbI_3$/NiO interface.

The reported Young's modulus of NiO (101-161 GPa[34] and 215 GPa[35]) is much higher than that of $MAPbI_3$ (13-22 GPa[36]) indicating a higher stiffness of NiO as compared to $MAPbI_3$. It is a

https://doi.org/10.1002/adma.201703879
Advanced Materials, 30, 5, 1703879 (2018)
clear indication that $MAPbI_3$ when deposited on NiO would not be able to deform the latter. Therefore, we used the relaxed lattice parameters of cubic NiO (Table S1) as the in-plane lattice constants of the interface model starting with the orthorhombic structure of $MAPbI_3$ as an initial guess. The resulting mismatch between the two structures is lower than 3% (Table S2) that is acceptable in semiconductor heterostructures and consistent with a coherent interface. This lattice matching of $MAPbI_3$ to cubic NiO induces a tetragonal constraint to $MAPbI_3$ resulting in a tetragonal like phase. This is in agreement with the crystalline tetragonal $MAPbI_3$ Bragg peaks measured in the diffraction data (Fig. 1c and S10).

The constructed interface model was allowed to relax along the stacking direction ($\mathbf{c_i}$) and the lateral in-plane parameters ($\mathbf{a_i}$ and $\mathbf{b_i}$) were kept constant as obtained from bulk NiO full relaxation (Tables S1-S2).

To combine NiO and $MAPbI_3$ at the interface, we tested different configurations of MA (Methyl-Ammonium) and iodine terminated $MAPbI_3$, which is the low energy termination of this structure[37]. In all cases, the relaxed interface leads to I atoms pointing towards Ni atoms in a similar way (Fig. S11-b), and the resulting Ni-I bond distances (~ 2.85-2.95 Å) are in good agreement with bulk Ni-I bond length (~2.78 Å) in hexagonal R-3m NiI_2[38]. Figure S11 shows one of the optimized interface models and the corresponding interface. The formation of Ni-I bonds at the interface is chemically consistent, since iodine is an anion that bonds to Ni, which is a cation. The superior photo-physical and electrical properties of $MAPbI_3$/LiNiO as compared to $MAPbI_3$/PEDOT: PSS is most probably related to the appropriate matching of NiO with $MAPbI_3$ resulting in a better valence band alignment that enhances hole transport. In addition, the appropriate matching between Li-NiO and $MAPbI_3$ contributes to the reduction of interface defect density ensuring the integrity of $MAPbI_3$ and lowering the surface states.

https://doi.org/10.1002/adma.201703879
Advanced Materials, 30, 5, 1703879 (2018)

Besides, we stress that PEDOT: PSS is a polymer that presents a disordered structure where the atomic positions are not well defined[39,40]. In addition to the surface roughness, such disordered structural motif is unlikely to afford a nice matching with $MAPbI_3$, contrarily to NiO (Fig. S11).

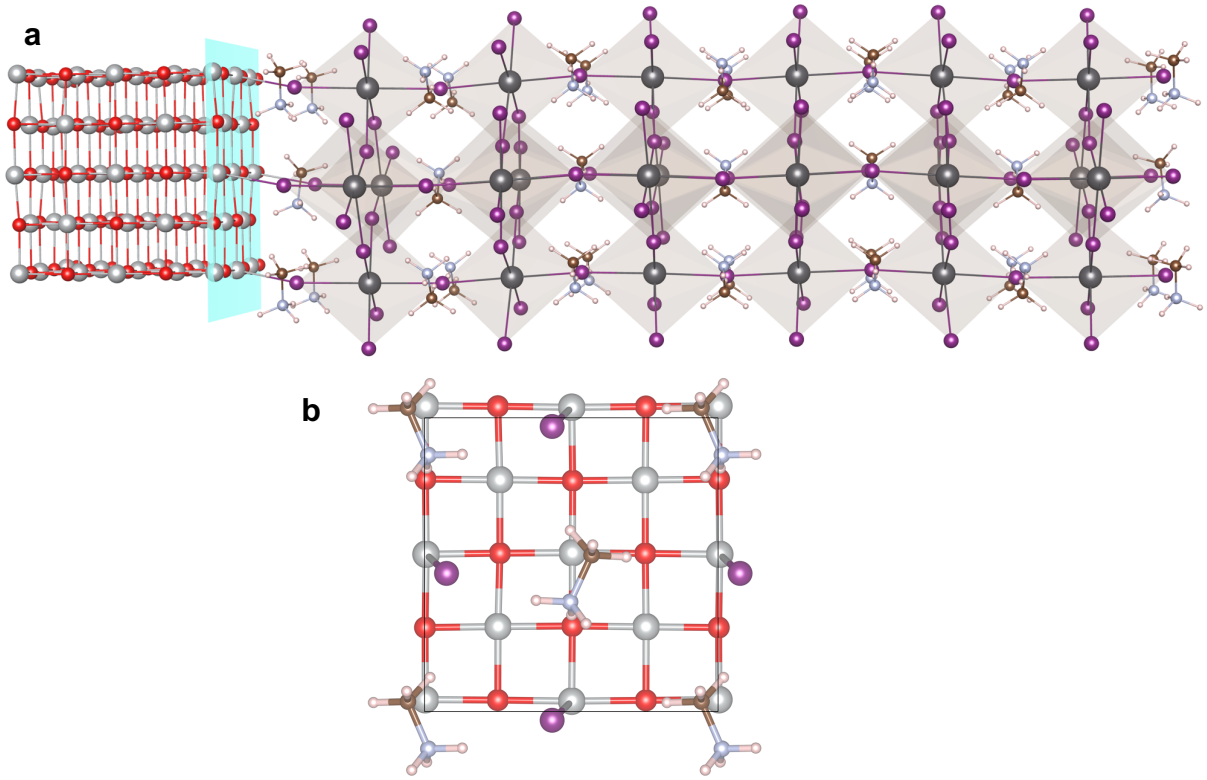

Figure S11. (a) Relaxed structure of the $MAPbI_3$/NiO model interface showing Ni-I bonds at the interface region. The shaded region at the interface shows the (100) plane of NiO. (b) Favored I positions at the interface where I atoms point towards Ni atoms. For the colors, red for O, gray for Ni, purple for I, light blue for N, brown for C and pink for H.

Photo-stability study

1. Crystallinity comparison between hot-casted and post-annealed $MAPbI_3$ grown on LiNiO

To compare the photo-stability for $MAPbI_3$ with different degree of crystallinity in the same device configuration, we grew $MAPbI_3$ on LiNiO under room temperature followed by a post-annealing process. Specifically, we spin coated the $MAPbI_3$ solution as described in the section Methods without pre-heating the substrate, to obtain a transparent film. Then the substrates were put on a

https://doi.org/10.1002/adma.201703879
Advanced Materials, 30, 5, 1703879 (2018)

100ºC hot-plate for 30min to convert the precursor into perovskite phase. The GIXRD pattern is shown in Fig. S12 with a comparative analysis on the peak indexing and width.

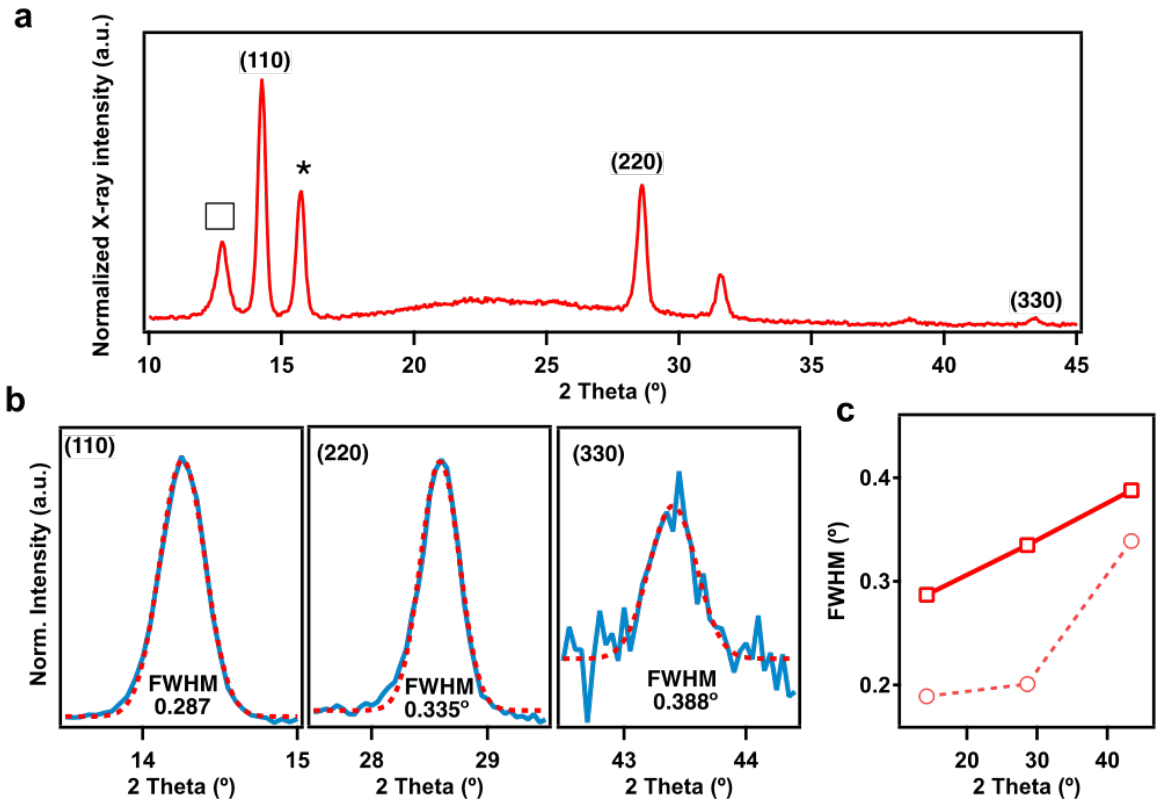

Figure S12. a, GIXRD pattern for post-annealed $MAPbI_3$ thin film grown on LiNiO without hot-casting method. b, The diffraction peaks zoomed in in specific region with Gaussian fit for FWHM. c, FWHM for each plane as a function of 2 Theta value, as a comparison, the data for hot-cast $MAPbI_3$ (data in Fig. 1 in MS) is shown as light red curve.

From this result, we found that the post-annealed $MAPbI_3$ on LiNiO using room temperature casting has much lower degree of crystallinity as revealed by the FWHM value and lack of peak splitting related to the tetragonal phase as observed by the hot-casting method on LiNiO.

We further used those post-annealed films on LiNiO for device fabrication in the same device configuration as the hot-casted $MAPbI_3$/LiNiO device studied in the manuscript for photo-stability

https://doi.org/10.1002/adma.201703879
Advanced Materials, 30, 5, 1703879 (2018)

tests. As shown in Fig. S13, the device undergoes the same photo degradation process under constant 1-Sun illumination. To make sure such degradation is photo-charging effect as described in Ref. 40 in the manuscript, we also test the recovery process by sitting the device in the dark (blue dots in Fig. S13). And the photocurrent can be recovered to higher value, which confirms such degradation induced by light is the same process as observed before in the $MAPbI_3$/PEDOT device case.

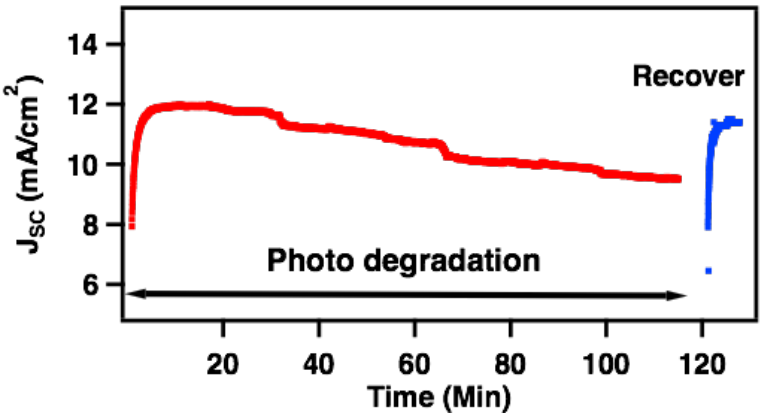

Figure S13. Photo-stability test for $MAPbI_3$ grown on LiNiO using room temperature casting

References

1. Street, R. A. Localized state distribution and its effect on recombination in organic solar cells. *Phys. Rev. B* **84**, 075208 (2011).
2. Hamilton, R. *et al.* Recombination in Annealed and Nonannealed Polythiophene/Fullerene Solar Cells: Transient Photovoltage Studies versus Numerical Modeling. *J. Phys. Chem. Lett.* **1**, 1432-1436 (2010).
3. Hohenberg, P. & Kohn, W. Inhomogeneous Electron Gas. *Phys. Rev.* **136**, B864-B871 (1964).
4. Kohn, W. & Sham, L. J. Self-Consistent Equations Including Exchange and Correlation Effects. *Phys. Rev.* **140**, A1133-A1138 (1965).
5. José, M. S. *et al.* The SIESTA method for ab initio order- N materials simulation. *J. Phys.: Condens. Matter* **14**, 2745 (2002).

6. Cooper, V. R. Van der Waals density functional: An appropriate exchange functional. *Phys. Rev. B* **81**, 161104 (2010).

7. Yuk, S. F. *et al.* Towards an accurate description of perovskite ferroelectrics: exchange and correlation effects. *Sci. Rep.* **7**, 43482 (2017).

8. Troullier, N. & Martins, J. L. Efficient pseudopotentials for plane-wave calculations. *Phys. Rev. B* **43**, 1993-2006 (1991).

9. Dudarev, S. L., Liechtenstein, A. I., Castell, M. R., Briggs, G. A. D. & Sutton, A. P. Surface states on NiO (100) and the origin of the contrast reversal in atomically resolved scanning tunneling microscope images. *Phys. Rev. B* **56**, 4900-4908 (1997).

10. Patterson, A. L. The Scherrer Formula for X-Ray Particle Size Determination. *Phys. Rev.* **56**, 978-982 (1939).

11. Scherrer, P. *Göttinger Nachrichten Gesell.*, Vol. 2 (1918).

12. Stokes, A. R. & Wilson, A. J. C. The diffraction of X rays by distorted crystal aggregates - I. *Proc. Phys. Soc.* **56**, 174 (1944).

13. Schoening, F. R. L. Strain and particle size values from X-ray line breadths. *Acta Crystallogr.* **18**, 975-976 (1965).

14. Halder, N. C. & Wagner, C. N. J. Separation of particle size and lattice strain in integral breadth measurements. *Acta Crystallogr.* **20**, 312-313 (1966).

15. J.I. Langford, i. S. B., C.R. Hubbard (Eds.). *Accuracy in Powder Diffraction*. NBS Special Publication No. 567, National Bureau of Standards, 1980, P. 255.

16. de Keijser, T. H., Langford, J. I., Mittemeijer, E. J. & Vogels, A. B. P. Use of the Voigt function in a single-line method for the analysis of X-ray diffraction line broadening. *J. Appl. Cryst.* **15**, 308-314 (1982).

17. Wiles, R. A. Y. a. D. I. Profile shape functions in Rietveld refinements. *J. Appl. Cryst.* **15**, 430-438 (1982).

18. Durand, O., Rogers, D., Teherani, F. H., Andrieux, M. & Modreanu, M. Studies of oxide-based thin-layered heterostructures by X-ray scattering methods. *Thin Solid Films* **515**, 6360-6367 (2007).

19. Almond, D. P. & Bowen, C. R. An Explanation of the Photoinduced Giant Dielectric Constant of Lead Halide Perovskite Solar Cells. *J. Phys. Chem. Lett.* **6**, 1736-1740 (2015).

20. Walter, T., Herberholz, R., Müller, C. & Schock, H. W. Determination of defect distributions from admittance measurements and application to Cu(In,Ga)Se2 based heterojunctions. *J. Appl. Phys.* **80**, 4411-4420 (1996).

21. Duan, H.-S. *et al.* The identification and characterization of defect states in hybrid organic-inorganic perovskite photovoltaics. *Phys. Chem. Chem. Phys.* **17**, 112-116 (2015).

22. Samiee, M. *et al.* Defect density and dielectric constant in perovskite solar cells. *Appl. Phys. Lett.* **105**, 153502 (2014).

23. Yin, L. *et al.* Limitation factors for the performance of kesterite Cu2ZnSnS4 thin film solar cells studied by defect characterization. *RSC Adv.* **5**, 40369-40374 (2015).

24. Michelson, C. E., Gelatos, A. V. & Cohen, J. D. Drive-level capacitance profiling: Its application to determining gap state densities in hydrogenated amorphous silicon films. *Appl. Phys. Lett.* **47**, 412-414 (1985).

25. Blancon, J.-C. *et al.* The Effects of Electronic Impurities and Electron–Hole Recombination Dynamics on Large-Grain Organic–Inorganic Perovskite Photovoltaic Efficiencies. *Adv. Funct. Mater.* **26**, 4283-4292 (2016).

26. Berberan-Santos, M. N., Bodunov, E. N. & Valeur, B. Mathematical functions for the analysis of luminescence decays with underlying distributions: 2. Becquerel (compressed hyperbola) and related decay functions. *Chem. Phys.* **317**, 57-62 (2005).

27. Pivrikas, A. *et al.* Bimolecular Recombination Coefficient as a Sensitive Testing Parameter for Low-Mobility Solar-Cell Materials. *Phys. Rev. Lett.* **94**, 176806 (2005).

28. Bi, C. *et al.* Non-wetting surface-driven high-aspect-ratio crystalline grain growth for efficient hybrid perovskite solar cells. *Nat. Commun.* **6**, 7747 (2015).

29. Ködderitzsch, D. *et al.* Exchange interactions in NiO and at the NiO(100) surface. *Phys. Rev. B* **66**, 064434 (2002).

30. Welton-Cook, M. R. & Prutton, M. LEED calculations for the NiO (100) surface: extension to lower energies. *J. Phys. C: Solid State Phys.* **13**, 3993 (1980).

31. Wyckoff R. W. G. *Crystal Structures* Vol. vol I (New York: Interscience, 1960).

32. Baikie, T. *et al.* Synthesis and crystal chemistry of the hybrid perovskite (CH3NH3)PbI3 for solid-state sensitised solar cell applications. *J. Mater. Chem. A* **1**, 5628-5641 (2013).

33. Hutchings, M. T. & Samuelsen, E. J. Measurement of Spin-Wave Dispersion in NiO by Inelastic Neutron Scattering and Its Relation to Magnetic Properties. *Phys. Rev. B* **6**, 3447-3461 (1972).

34. Fasaki, I., Koutoulaki, A., Kompitsas, M. & Charitidis, C. Structural, electrical and mechanical properties of NiO thin films grown by pulsed laser deposition. *Appl. Surf. Sci.* **257**, 429-433 (2010).

35. Shen, Y. F., Xue, W. Y., Wang, Y. D., Liu, Z. Y. & Zuo, L. Mechanical properties of nanocrystalline nickel films deposited by pulse plating. *Surf. Coat. Technol.* **202**, 5140-5145 (2008).

36. Berry, J. *et al.* Hybrid Organic–Inorganic Perovskites (HOIPs): Opportunities and Challenges. *Adv. Mater.* **27**, 5102-5112 (2015).

37. Quarti, C., De Angelis, F. & Beljonne, D. Influence of Surface Termination on the Energy Level Alignment at the CH3NH3PbI3 Perovskite/C60 Interface. *Chem. Mater.* **29**, 958-968 (2017).

38. Wyckoff, R. W. G. *Cadmium Iodide Structure. Crystal Structure* Second Edition edn, Vol. 1 239-444 (Interscience Publishers, New York Note., 1963).

39. Rivnay, J. *et al.* Structural control of mixed ionic and electronic transport in conducting polymers. *Nat. Commun.* **7**, 11287 (2016).

40. Lenz, A., Kariis, H., Pohl, A., Persson, P. & Ojamäe, L. The electronic structure and reflectivity of PEDOT:PSS from density functional theory. *Chem. Phys.* **384**, 44-51 (2011).